Report Title: *Final Report - Center for Renewable Energy Science and Technology*

Type of report: Scientific

Reporting period start date: January 1, 2011

Reporting end date: January 15, 2013

Principal authors: Dr. Richard E. Billo. (richard.billo@uta.edu)
Dr. Krishnan Rajeshwar (rajeshwar@uta.edu

Date of Report was issued: April 15, 2013

DOE Award Number: DE-FE0002829

Submitting organization: The University of Texas Arlington
Box 19015
Arlington, TX 76019-0145

Disclaimer:

Abstract:

The CREST research team conducted research that optimized catalysts used for the conversion of southwestern lignite into synthetic crude oil that can be shipped to nearby Texas refineries and power plants for development of transportation fuels and power generation. Research was also undertaken to convert any potential by-products of this process such as CO_2 to useful chemicals and gases which could be recycled and used as feedstock to the synthetic fuel process. These CO_2 conversion processes used light energy to drive the endogonic reduction reactions involved.

The project was divided into two tasks: A CO_2 Conversion Task, and a Catalyst Optimization Task. The CO_2 Conversion task was aimed at developing molecular and solid state catalysts for the thermal, electro- and photocatalytic reduction of CO_2 to reduced products such as simple feedstock compounds (e.g. CO, H_2, CHOOH, CH_2O, CH_3OH and CH_4). For example, the research team recycled CO that was developed from this Task and used it as a feedstock for the production of synthetic crude in the Catalyst Optimization Task.

In the Catalyst Optimization Task, the research team conducted bench-scale experiments with the goal of reducing overall catalyst cost in support of several synthetic crude processes that had earlier been developed. This was accomplished by increasing the catalyst reactivity thus reducing required concentrations or by using less expensive metals. In this task the team performed parametric experiments in small scale batch reactors in an effort to improve catalyst reactivity and to lower cost. They also investigated catalyst robustness by testing lignite feedstocks that vary in moisture, ash, and volatile content.

TABLE OF CONTENTS

EXECUTIVE SUMMARY

The CREST research team conducted research that optimized catalysts used for the conversion of southwestern lignite into synthetic crude oil that can be shipped to nearby Texas refineries and power plants for development of transportation fuels and power generation. Research was also undertaken to convert any potential by-products of this process such as CO_2 to useful chemicals and gases which could be recycled and used as feedstock to the synthetic fuel process. These CO_2 conversion processes used light energy to drive the endogonic reduction reactions involved. The project was divided into two tasks which are summarized below. In addition, Task 1, a Project Management task was consistently carried out to ensure consistency to budget, objectives, and time requirements, as well to ensure safe practices were carried out throughout the project.

Task 2: CO_2 Conversion

CO_2 is an unavoidable by-product from any fossil fuel combustion process. Due to the environmental concerns about continued CO_2 emissions into the atmosphere, technologies for the conversion of CO_2 to useful, environmentally friendly products is paramount. Other than sequestration, the only feasible long term solution is the reduction of CO_2 into useful fuels, (i.e. alcohols and hydrocarbons). Such technology could greatly reduce CO_2 emissions or even close the carbon cycle – a carbon-neutral fuel cycle with respect to the atmosphere. This task was aimed at developing molecular and solid state catalysts for the thermal, electro- and photocatalytic reduction of CO_2 to reduced products such as simple feedstock compounds (e.g. CO, H_2, CHOOH, CH_2O, CH_3OH and CH_4). For example, we recycled CO that was developed from this Task and used it as a feedstock for the production of synthetic crude in Task 3.

Task 3: Catalyst Optimization

Several processes for converting lignite into synthetic crude (syncrude) were investigated by our group in the past three years. During this time, we developed a cost effective approach that used a catalytic reaction conducted under moderate temperature and pressure conditions. Our ultimate goal was to bring this process to a pilot scale somewhere close to a lignite mine in Texas. In support of this effort, we conducted bench-scale experiments with the goal of reducing overall catalyst cost. This was accomplished by increasing the catalyst reactivity thus reducing required concentrations or by using cheaper metals. In this task we performed parametric experiments in small scale batch reactors in an effort to improve catalyst reactivity and to lower cost. We also investigated catalyst robustness by testing lignite feedstocks that vary in moisture, ash, and volatile content.

Task 1: Project Management

The project management task consisted of leading and coordinating the project tasks. This included risk management, providing support to successfully accomplish technical project milestones, review meetings, budgets, cost reports, and reports (quarterly, yearly and final). We conducted weekly 2-hour research status meetings for the project. In this meeting, a roundtable discussion of experimental results from the previous week's efforts was conducted. Various ideas were generated for pursuit of the following week's activities for each task of the project. In addition, information was communicated for deadlines for quarterly reports, report formats, budget status, schedule status, students assigned to the project, and other such matters are discussed. This project team has successfully worked together for several years, which enabled this task to be completed successfully on time and on budget.

In addition, on a quarterly basis, safety inspections of the laboratories used for the project were conducted by the university's Environmental Quality and Safety Department. These inspections included assessment of adherence to safe hydrogen usage and storage, chemical usage and storage, and adherence to laboratory cleanliness and emergency procedures adherence. Any concerns resulting from inspections were addressed and corrected within university guidelines to corrections.

Task 2: CO_2 Conversion

2.1. Coupling Molecular Photocatalysts with an Electrode for Photoelectrocatalysis

The catalytic reduction of carbon dioxide (CO_2) to fuels and organic compounds using light, electricity, or a combination of both, is not a new topic. References to this topic date back to the 1800s, although rapid progress was made only since the 1970s. A major challenge relates to the fact that the CO_2 molecule is extremely stable and is kinetically inert.

For photochemical reduction in an homogeneous system, the chromophores $[Ru(phen)_3]^{2+}$ and $[Ru(bpy)_3]^{2+}$ still represent the most widely used systems for driving highly endogonic redox reactions, due to their excited state energetics and good chemical stability. Particularly, the $[Ru(phen)_3]^{2+}$ complex has been the primary one used in our studies on homogeneous photochemical reduction of CO_2. As shown schematically in **Figure 2.1.1**, the reduction potential for both the photoexcited state $[Ru(phen)_3]^{2+*}$ or the reductively quenched chromophore $[Ru(phen)_3]^{+}$ are negative of the key CO_2 reduction couples, meaning that these species are thermodynamically capable of reducing CO_2. Given that the redox potentials for most of the CO_2-derived reduction processes lie negative of the hydrogen evolution reaction (HER) in water (the two exceptions being the deep reduction of CO_2 to methanol and methane), the more negative the ruthenium complex photoexcited state is, the better is the expected performance under solar light because the thermodynamic driving force for the reduction is roughly given by the difference between the LUMO energy levels and the corresponding CO_2 redox potential. Thus the more negative the LUMO energy level is, the greater the driving force all other factors being equal. However, it is worth emphasizing that such thermodynamic arguments are only starting points.

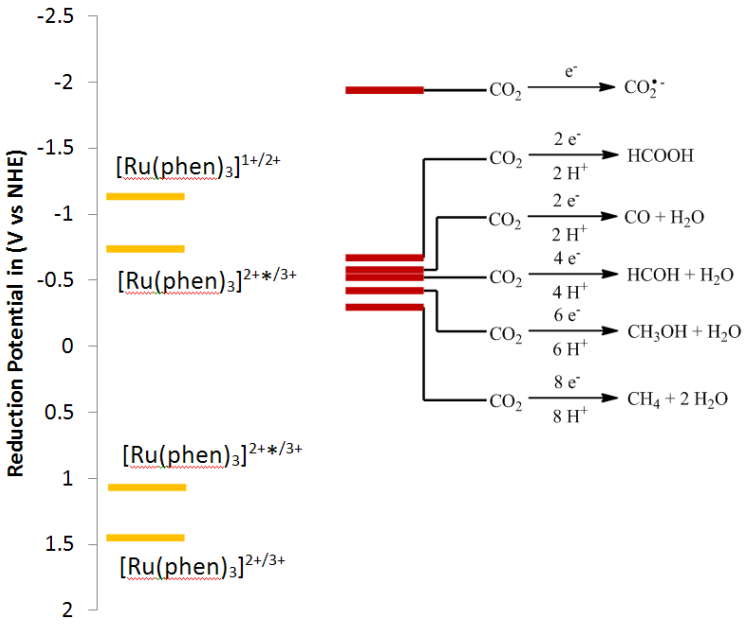

Figure 1.2.1. Reduction potentials of carbon dioxide reduction as compared with the HOMO and LUMO levels of $[Ru(phen)_3]^{2+}$ chromophore.

The rate of the reaction between the photoexcited $[Ru(phen)_3]^{2+*}$ and CO_2, depends on the reactant concentrations, the photon flux, the lifetime of the excited state complex and, importantly, the ability of the excited-state complex to transfer an electron to the CO_2. These simple complexes lack the chemical functionality to lower the activation barriers involved and are only capable of delivering a single electron each towards these multi-electron reactions. It is also worth noting that the initial conversion of CO_2 to CO is the energy "hog" in the overall process and consumes a minimum of 1.33 eV. Much of the progress associated with the conversion of CO_2 to CO and formate has revolved around electro- and photocatalytic strategies for minimizing the additional overpotential over and above this minimum threshold.

Although many homogeneous catalysts have been developed for both electrochemical and photochemical systems, only few are capable of deeper reduction than the two-electron reduced products of CO_2, such as CO and formic acid. We found out that out of 72 molecular electrocatalytic systems for CO_2 reduction, 71 are metal complexes and the final product in the majority is CO, representing only a net two electron reduction of CO_2. The sole organic electrocatalyst is pyridine and this simple molecule is able to catalyze even deeper CO_2 reduction to products including methanol at very low reducing potentials (E. Barton-Cole, P. S. Lakkaraju, D. M. Rampulla, A. J. Morris, E. Abelev and A. B. Bocarsly, *Journal of the American Chemical Society*, 2010, **132**, 11539-11551). In this system, the electrocatalyst is the pyridinium cation, which upon reduction can bind CO_2 to form carbamate-type adducts and, via redox cycling, shuttles six electrons to ultimately form methanol, as shown in **Figure 2.1.2**. Through simulation of experimental results and kinetic studies, they were able to deduce the possible mechanism of the reduction of CO_2 to methanol. The electron transfer in this process proceeds through an inner sphere electron transfer as was shown by $^{13}C^{15}N$ coupling in NMR and by gas-phase photoelectron spectroscopy. Based on the calculated bond distance and bond angles the nature of the N-CO_2 bond was found to be primarily of π-character as opposed to σ-character. Reductions beyond the first

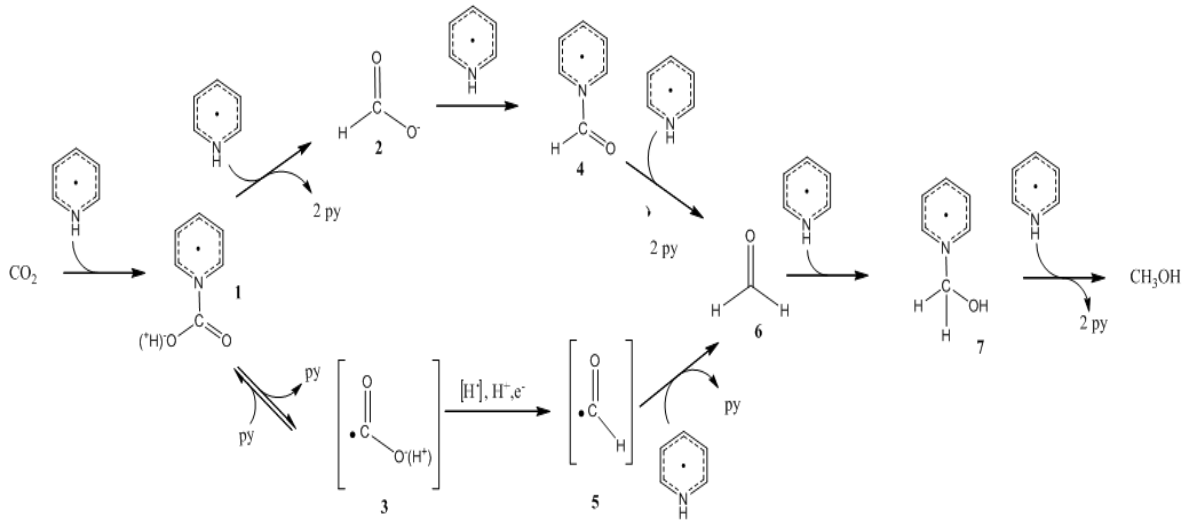

Figure 2.1.2. Pyridinium catalyzed reduction of carbon dioxide.

electron transfer were found to depend on the electrodes being used. For electrodes with low hydrogen potential, such as Pt or Pd, it was found that dissociation of the pyridine-formate radical adduct occurs, allowing the next reduction to formate or formic acid to take place on the electrode surface. For electrodes with high hydrogen potential, the reaction is catalyzed entirely by the pyridinium with no dissociation of the formate radical, but a second pyridinium radical passes an electron to the pyridine-formate radical adduct instead as shown in **Figure 2.1.2**. With low hydrogen potential electrodes, formic acid adsorbs onto the surface to produce the hydroxyformyl radical that reacts with a surface hydrogen atom to make the formyl radical which is finally reduced by the pyridinium radical to formaldehyde, bottom of **Figure 2.1.2**. For high hydrogen potential electrodes, formic acid reacts with the pyridinium radical to make the pyridinium-formyl adduct which is further reduced by a second pyridinium radical to form free formaldehyde and two equivalents of pyridine, top of **Figure 2.1.2**. The reduction of formaldehyde for both electrode types results from its reaction with a pyridinium radical to form an intermediated species en route to methanol, and this species reacts with a second pyridinium to produce methanol and two equivalence of pyridine. There is some debate about this mechanism proposed by Bocarsly et al. and with some groups claiming a non-innocent role of the electrode surface in the process and thus a process which is necessarily heterogeneous.

We have examined the homogeneous photochemical of CO_2 using a $[Ru(phen)_3]^{2+}$ chromophore and pyridine as a co-catalyst in aqueous solution. We hypothersized that the photoexcited chromophore could take the place of the reducing electrode and drive the pyridine catalyzed CO_2 to methanol reaction. This idea was based on the expected capability of the photoexcited state $[Ru(phen)_3]^{2+}$* to transfer an electron to protonated pyridinium cation **pyH$^+$** (formed in solution at pH $\leq$ 5.5 thus generating a pyridinium radical which is the key participant to react with dissolved CO_2 and convert it to methanol. In this system, ascorbic acid was used as sacrificial donor to enhance the electron transfer from the excited $[Ru(phen)_3]^{2+}$* chromophore to the **pyH$^+$** cation. In an ideal photocatalytic system, this donor would be replaced by water oxidation catalysts and the oxidative by-product would be O_2, as shown in reaction 1. By using a sacrificaial donor we can by-pass the technical problems associated with the water oxidation reaction (see reaction 2) and focus exclusively on the reductive chemistry (reaction 3). In electrochemically driven catalysis, reactions 2 and 3 occur at spatially separated electrodes, so it is reasonable to address the two half-reactions involved as separate research problems, to be combined later in a photoelectrochemical system

This reduction reaction 3 requires a total of 6 photons to generate 6 excited electrons for completion. of one catalytic cycle. Fortunately, the 6 one-electron steps required for the CO_2 reduction are a good match for the one-photon, one electron stoichiometry associated with photoexcitation of a molecular chromophore.

Fuel Formation Reaction: $CO_2 + 2\,H_2O \rightarrow CH_3OH + 3/2\,O_2$ (1)

Oxygen Evolving Reaction (OER): $H_2O \rightarrow 4\,H^+ + 4\,e^- + O_2$ (2)

CO_2 Reduction Reaction (CRR): $CO_2 + 6\,e^- + 6H^+ \rightarrow CH_3OH + H_2O$ (3)

Typical **D**'s include triethylamine (TEA) and triethanolamine (TEOA) for neutral and basic solutions and ascorbic acid (AA) and ascorbate (A^-) for acidic solutions. While these donors usually work quite well and are widely adopted for photochemical studies with ruthenium polypyridyl and related chromophores, however it is not always clear that the oxidation products are completely innocent. For example, TEA^+ is known to rapidly deprotonate to form a neutral carbon centered radical species which itself is a potent reductant. If this neutral radical species further reduces the substrate, the product yield will be artificially high. Because of this, turnover numbers or quantum yields generated in this type of study should only be considered as an upper-limit.

As shown in **Figure 2.1.3**, this photocatalytic system is functional and produces methanol for a period of ~ 6 hours before the activity ceases. Methanol detection was done by gas chromatography (GC) using either an FID or a MS detector. As shown in **Figure 2.1.3**, methanol was seen to increase consistently under continuous mono-chromatic irradiation of a CO_2 saturated aqueous solution of $[Ru(phen)_3]^{2+}$, pyridine, and ascorbic acid in water (pH 5.0). The light irradiation was maintained for a period of six hours after which it was interrupted because the amount of methanol was seen to reach a plateau. Monochromatic light of 470 nm (equivalent to 2.65 eV) was chosen to singly excite the $[Ru(phen)_3]^{2+}$ to $[Ru(phen)_3]^{2+*}$ involving to pump up electron from the $d\pi(Ru)$ to the π_1^* energy levels.

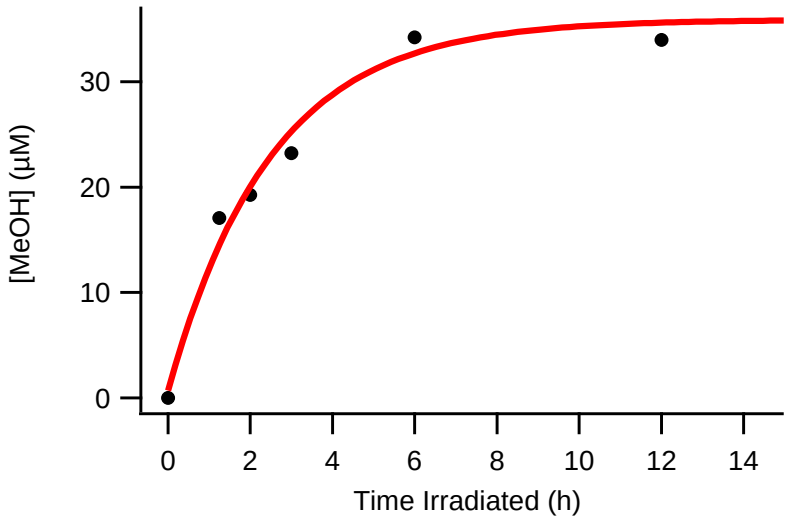

Figure 2.1.3 Temporal evolution of methanol generated in a CO_2 saturated aqueous solution (pH 5.4) under continuous monochromatic irradiation (470 nm) and containing $[Ru(phen)_3]^{2+}$, pyridine and ascorbic acid.

We propose that the photoexcited $[Ru(phen)_3]^{2+*}$ reacts directly with $\mathbf{pyH^+}$ ($E^0_{pyH+/0}$ = -0.38 V vs NHE) to form the radical $\mathbf{pyH}^{\cdot}$ and $[Ru(phen)_3]^{3+}$ which is rapidly reduced by sacrificial reductants or donors (**D**) to complete the catalytic cycle with respect to Ru. The $\mathbf{pyH}^{\cdot}$ generated in this step can go on to react with CO_2 and in successive one-electron steps get reduced to CH_3OH, as was shown in **Figure 2.1.2.**

The mechanism of CO_2 reduction via reaction of the chromophore with pyridine in CO_2 saturated aqueous solutions is indicated in **Figure 2.1.4**; the entire system is simply seen to be a combination of the CO_2-reducing ability of pyridine and the reducing power of $[Ru(phen)_3]^+$ formed upon reductive quenching of the ^{3}MLCT state in the complex. Importantly, *this is the first experimental corroboration of pyridine functioning to produce methanol in a purely molecular system.* At present, the photoactivity of the $[Ru(phen)_3]^{2+}$/pyridine system is modest with 0.15 methanol molecules per Ru chromophore over a 6 h period. When adjusted for the number of electrons involved, comes to 0.9 TON, before the system becomes inactive. The loss of activity is presumably due to photodegradation of the chromophore. In non-aqueous systems these kinds of chromophores generally last ~12 h before appreciable decomposition, but water speeds up this process.

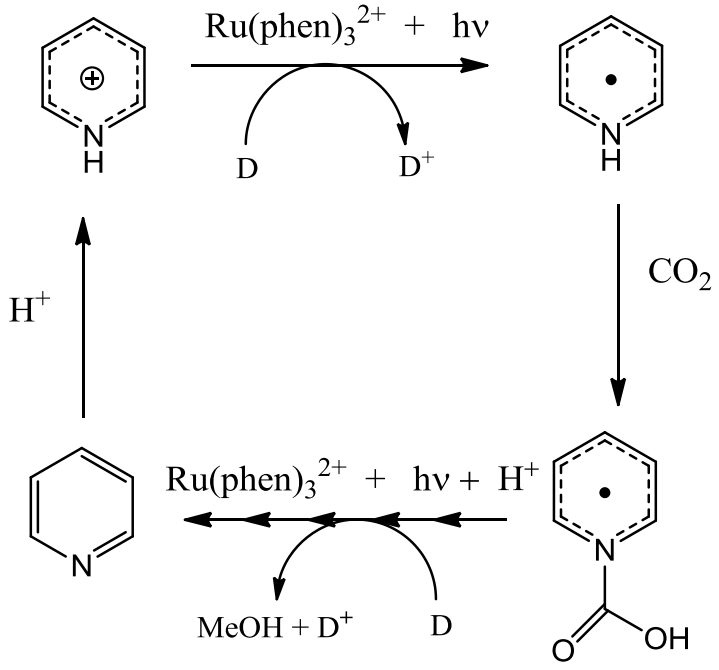

Fig. 2.1.4 Proposed mechanism of the reduction of CO_2 by pyridine in the presence of $[Ru(phen)_3]^{2+}$ chromophore in aqueous solution saturated with CO_2 and irradiated with monochromatic light of 470 nm.

Ruthenium polypyridyl complexes for electrocatalytic and photocatalytic reduction of CO_2

Several ruthenium polypyridyl complexes have been explored as candidates for electrocatalytic CO_2 reduction. Among them, the most important are $Ru(phen)_2(CO)_2^{2+}$ and $Ru(bpy)_2(CO)_2^{2+}$. These complexes typically make CO, H_2, and formate as products of reduction (H. Ishida, K. Fujiki, T. Ohba, K. Ohkubo, K. Tanaka, T. Terada and T. Tanaka, *Journal of the Chemical Society, Dalton Transactions*, 1990, 2155-2160; H. Ishida, T. Terada, K. Tanaka and T. Tanaka, *Inorganic Chemistry*, 1990, **29**, 905-911) with the ratio of these products being pH dependent. At pH 6, the products are CO and H_2; however at pH 9.5, formate is produced in addition to CO and H_2.

Compared to electrocatalysts for CO_2 reduction, molecule-based photochemical systems capable of photoreducing CO_2 beyond formic acid or CO are hard to come by. Therefore newly formulated photocatalysts and/or electrocatalysts are urgently needed to convert CO_2 to useful products. With this end, we focused on the synthesis of at least 500 mg of a number of appropriately modified phenanthroline ligands, which are required for the catalyst preparation. The ligands dppz, pbtpα, and pbtpβ were chosen

to be the receptacle of the photoelexcited electrons from a Ruthenium chromophre. The ligands were prepared via the condensation reaction of 1,10-phenanthroline-5,6-dione (phendione)with the 1,2-diaminobenzene, 2,3-diaminopyridine, and 3,4-diaminopyridine, respectively. The ruthenium complexes of these ligands were prepared by the similar condensation reaction between $[(phen)_2Ru(phendione)]Cl_2$ and 1,2-diaminobenzene, 2,3-diaminopyridine, and 3,4-diaminopyridine, respectively. In a similar manner, we have begun to prepare the ruthenium complexes required for this proposal.

Based on 500 mg phendione, yields of dppz, pbtpα, and pbtpβ were between 550 to 600 mg, each (~95%). The free ligands were characterized by ^{1}HNMR and mass spectrometry. In a typical procedure, 1.3 g (1.75 mmol) of $[Ru(phen)_2$ phendione$]Cl_2$ was dissolved in 50 mL ethanol and 0.5 mL acetic acid. To this solution, 1.9 mmol of the respective diamine dissolved in 10 mL ethanol was added in one portion and the resulting solution refluxed for 6 h. Yields were typically between 80 and 85 %. The ^{1}H NMR data for these three complexes are listed below:

$[Ru(phen)_2dppz](PF_6)_2$ ^{1}H NMR (MeCN-d_3): δ 9.61 (dd, 2H), δ 8.60 (dd, 4H), δ 8.45 (dd, 2H), δ 8.25 (s, 4H), δ 8.21 (dd, 2H), δ 8.11 (m, 4H), δ 8.01 (dd, 2H), δ 7.75 (dd, 2H), 7.63 (m, 4H);

$[Ru(phen)_2pbtpα](PF_6)_2$ ^{1}H NMR (MeCN-d_3): δ 7.62 (m, 4H); δ 7.77 (dd, 2H), δ 8.01 (d, 2H), δ 8.08 (dd, 1H), δ 8.12 (dd 2H), δ 8.21 (dd,2H); δ 8.25 (s, 4H), δ 8.61 (m, 4H), δ 8.82 (dd, 1H), δ 9.45 (dd, 1H), δ 9.60 (d, 1H); δ 9.67 (d, 1H);

$[Ru(phen)_2pbtpβ](PF_6)_2$ ^{1}H NMR (MeCN-d_3): δ 7.64(m, 4H), δ 7.77(m, 1H), δ 8.00(dd, 2H), 8.12 (td, 2H); δ 8.20 (d, 2H), δ 8.25 (s, 4H), δ 8.28 (d, 1H), δ 8.61 (dd, 4H); δ 9.05 (d, 1H), δ 9.62(dd, 2H), δ 9.89 (s, 1H).

Once we prepared the modified phenanthroline ligands, dppz, pbtpα, and pbtpβ, required for the ruthenium catalyst preparation, the related ruthenium photocatalysts $[Ru(phen)_2dppz](PF_6)_2$, $[Ru(phen)_2pbtpα](PF_6)_2$, and $[Ru(phen)_2pbtpβ](PF_6)_2$ were all prepared and structurally characterized using a combination of NMR, mass spectrometry and elemental analyses (**Figure 2.1.5**). From now on, the $[Ru(phen)_2dppz](PF_6)_2$, $[Ru(phen)_2pbtpα](PF_6)_2$, and $[Ru(phen)_2pbtpβ](PF_6)_2$ will henceforward nominated **Rudppz**, **Ruα** and **Ruβ** respectively.

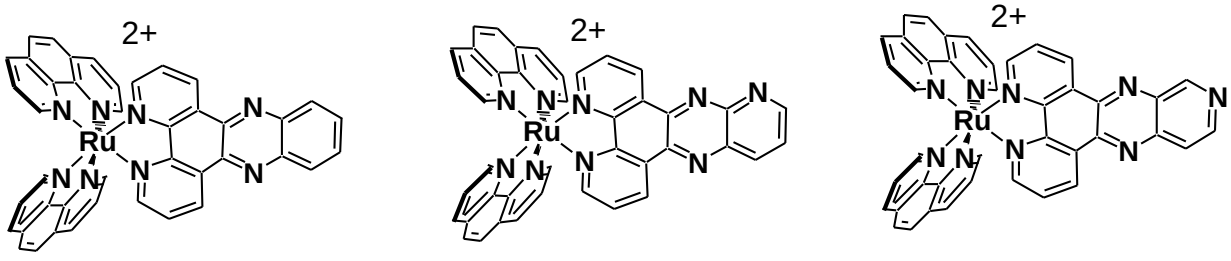

$[(phen)_2Ru(dppz)]^{2+}$ **Rudppz**

$[(phen)_2Ru(ptpbα)]^{2+}$ **Ruα**

$[(phen)_2Ru(ptpbβ)]^{2+}$ **Ruβ**

Fig.2.1.5 Structures of $[(phen)_2Ru(ptpbα)]^{2+}$ and $[(phen)_2Ru(ptpbβ)]^{2+}$ complexes and their precursor $[(phen)_2Ru(dppz)]^{2+}$ complex.

It is well-established that the energies of MLCT absorption in most Ru(II) polypyridyl complexes correlate linearly with the difference between the electrochemical potentials for (metal-centered) oxidation and (ligand centered) reduction. In these cases, the redox MO and the optical MO are the same. In complexes with laminate acceptor ligands, it is generally the second or third reduction potential that reveals the energy of the optical MO and these values are perturbed to more negative potentials than anticipated due to Coulombic effects. Laminate acceptor ligands have two or more acceptor orbitals that are delocalized over the entire ligand (laminated over each other) but interact with the metal such that one orbital defines the ground state optical properties of the complex (referred to as the 'optical' molecular orbital) and the other orbital defines the ground state reduction potentials (referred to as the 'redox' molecular orbital). Nonetheless, the difference in the $Ru^{2+}/^{3+}$ potential and the reduction potential of the proximal (or optical) MO does correspond well with the optical data ($^1MLCT_{prox}$ typically centered at ~ 460 nm). The observation of the redox MO reduction prior to reduction of the optical MO is a clear measure that the redox MO is the ground state LUMO.

To ascertain the energy levels of these ruthenium complexes, differential pulse voltammetry, DPV, runs are compared for these three chromophores complexes in dimethylformamide (DMF) solvent containing 0.1 M tetrebutylammonium hexafluorophosphate as supporting electrolyte **(Figure. 2.1.6)**. As references, DPV runs of $[Ru(phen)_3]^{2+}$ and pyridine are also included in the figure. All compounds were compared at same concentration (500 μM) and under same voltammetric parameters (potential pulse amplitude = 0.05 V, step size = 0.004 V, pulse duration = 0.05 s and pulse period =0.2 V).

The first electroreduction processes for **Rudppz**, **Ruα** and **Ruβ** in N_2- saturated DMF:H_2O (1M, pH 5.5) showed highly reversible voltammetric waves (v = 50 mV/s) and redox potentials, E^0, of -0.80 V, -0.64 V and -0.58 V vs. Ag/AgCl respectively. Although the redox process for each of **Ruα** and **Ruβ** complexes is expected to be localized on the redox-orbital of the dppz-type ligand, the respective E^0 values are observed at potentials more positive than that for the first electroreduction of **Rudppz** (-0.81 V vs. Ag/AgCl) in dry DMF which shifts slightly to –0.80 V after addition of traces of water. Accordingly, the DPV cathodic peak of each complex is seen in **Figure 2.1.6** to move progressively to less negative potentials from the **Rudppz**, (magenta trace) then **Ruα** (green trace) and finally **Ruβ** (red trace) indicating that **Ruβ** is expected to be the best electrocatalyst for CO_2 reduction because of the lower bias required to insert an electron in its ptpbβ ligand. This electron will be occupying an orbital involving the farthest nitrogen in the compound, and therefore called "distal" (redox) molecular orbital.

It is also important to compare the first electroreduction process of these three **Rudppz**, **Ruα** and **Ruβ** complexes with that of the $[Ru(phen)_3]^{2+}$ complex, the latter showing the first electron uptake at ca. -1.2 V with is associated to the proximal molecular orbital. Therefore, in **Rudppz**, **Ruα** and **Ruβ** complexes the first electroreduction (filling the distal MO) is apparently pushing the next electron uptake to more negative values than those observed $[Ru(phen)_3]^{2+}$ complex thus signaling a shift of the energy level corresponding to the proximal MO in the laminate ligands.

The most contrasting situation is found when comparing the DPV traces of the four ruthenium complexes (**Figure 2.1.6 # and a-c**) with that of pyridine (**Figure 2.1.6 ♦**), as pyridine is not showing any electroreduction peak in the -0.1 V to -1.6 V potential range. As these runs were obtained with a glassy carbon working electrode, the inactivity of pyridine is in agreement with reported data indicating that pyridine requires a noble metal electrode to show a reversible redox process at -0.58 V. However, when pyridine is included in a laminate ligand as thse in these ruthenium complexes, it is able to show normal electrochemical activity under rather low potentials.

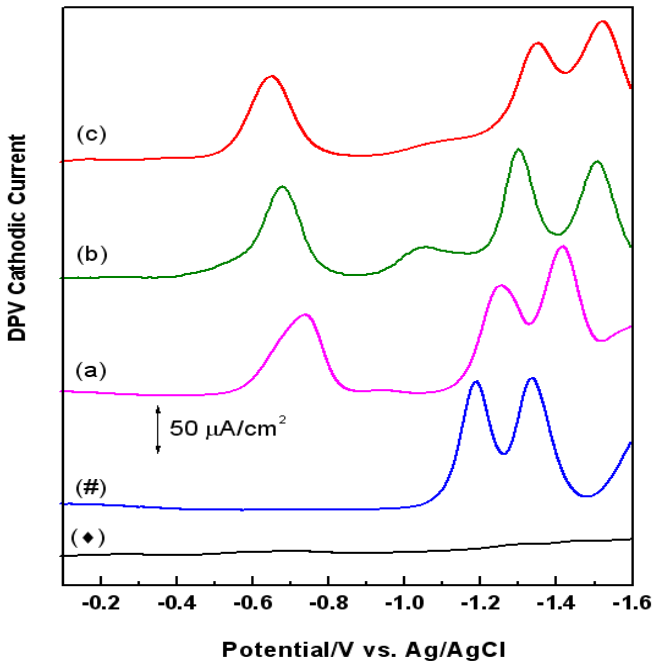

Figure 2.1.6 Comparison of DPV runs for the electroreduction of Rudppz (a), Ruα (b), and Ruβ (c) in DMF/H2) (1M, pH 5.5) solutions saturated with N_2. DPV runs for $[Ru(phen)_3]^{2+}$ (#) and pyridine (♦) are also included for comparison. Working electrode = GC (1 mm diameter). Supporting electrolyte = 0.1 M $TBAPF_6$.

After one electron uptake (first electroreduction peak), it is worth noticing that DPV profile of complex **Ruα** (**Figure 2.1.6** green trace) shows a clear second process at ca. -1.0V suggesting a follow-up reaction of the radical cation $[(phen)_2Ru^{II}(ptpb\alpha^{\bullet-})]^{+}$ which after being formed at the main electroreduction process is able to produce a species that is reduced in a separate and smaller wave located more negatively. This follow-up reaction, more neatly depicted at low scan rates (data not shown), is signaling the formation of a dimer chemically generated from the radical cation.

We demonstrated that the **Ruα** and **Ruβ** complexes are competent electrocatalysts for CO_2 reduction to methanol in dimethylformamide (DMF) solvent containing 1 M water. The low amount of water is required to provide aqueous protons in the conversion of CO_2 to CH_3OH. The electrocatalytic reduction of CO_2 can be observed by simply bubbling CO_2 through the system and examining the effect on the CVs, particularly those performed at low potential scans (5-10 mV/s). As shown in **Figure 2.1.7**, large increases in the cathodic current for both **Ruα** and **Ruβ** occur when CO_2 is added to the solution pointing out to a catalytic wave of the CO_2 reduction at -0.64 V and -060 V respectively. On the contrary only small changes are observed on the CV for **Rudppz** when CO_2 is added (data not shown). On purpose, the runs were conducted at a low scan rate (5 mV/s) to enhance the effect of the follow-up chemical reaction of the first reduced product with CO_2. This is clearly manifested on the returning positive-going scan showing anodic currents much smaller than those shown in the absence of CO_2. This behavior points out to a catalytic chemical reaction of CO_2 with the reduced product of any of the complexes (catalytic EC'-type). Besides, a voltammetric run in CO_2-saturated solution without addition of any of the ruthenium complexes (black dot trace in **Figure 2.1.7**) indicates that the glassy carbon electrode does not show itself any catalytic activity for CO_2 reduction. In fact, the electroreduction of CO_2 in media of low proton availability (DMF, DMSO) was reported to occur at very negative potentials (-2.16 V vs. Ag/AgCl) and involve competitive pathways originating from CO_2 electroreduction to $CO_2^{\bullet-}$ and involving formation of $C_2O_4^{2-}$, and CO, as well as $HCOO^-$ in the presence of residual or added water. Therefore, both **Ruα** and **Ruβ** are good electrocatalysts performing the reduction of CO_2 at ca. -1.60 V lower potentials than in their absence.

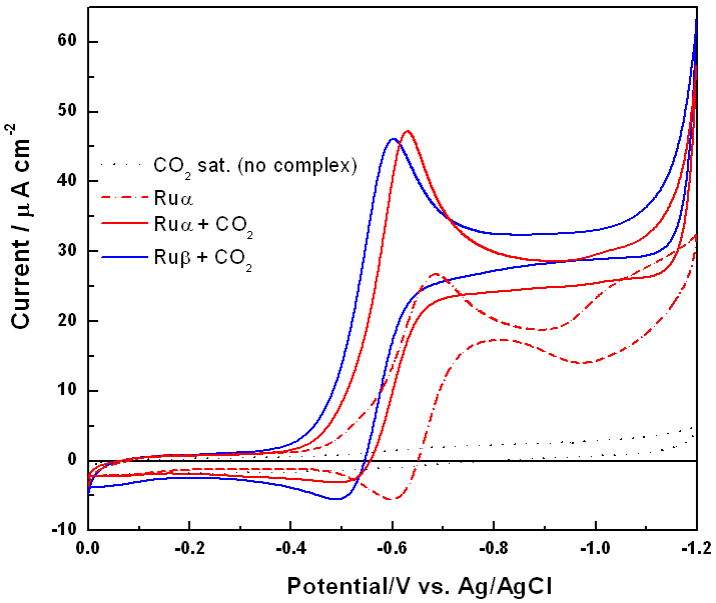

Figure 2.1.7 Comparison of the voltammetric behavior of **Ruα** (red solid line) and **Ruβ** (blue solid line) in DMF/H_2O (1 M, pH 5.5) solutions saturated with CO_2. Voltammograms of **Ruα** before saturation with CO_2 (red dash line) and that without Ru complex but with CO_2 (black dot line) are included as reference. All voltammograms were run at 5 mV/s using a glassy carbon disk (1 mm dia.) as working electrodeelectrod

It is worth noticing that the voltammetric behavior of both complexes in CO_2-saturated solutions is similar in shape although **Ruβ** shows a cathodic peak at less negative potentials than its **Ruα** analog indicating a more facile interaction with CO_2 for

the first complex. In both cases, the presence of a reactive nitrogen site on the ptpb (either α or β) ligand facilitates the formation of a CO_2 adduct, presumably in the form of a carbamate-type intermediate. **Figure 2.1.7** also shows a net increase of cathodic current at potentials more negative than -1.1 V for both complexes, indicating that the reduction CO_2 is also catalytically occurring at these potentials (as shown by the comparison with the voltammogram of CO_2 in the absence of the complex, dot line curve). This is important in the view of the photochemical reduction of CO_2 as the ^{1}MLCT excitation of the Ru π→ ptpb dπ band in any of the complexes and reductive quenching of the ^{3}MLCT excited state by TEA could trap the electron on the ligand ptpb to form $[(phen)_2Ru^{II}(ptpb^{\bullet-})]^+$ either in the bpy structure of the ptpb or at the farther N of the structure. The two different locations in the ptpb ligand might work properly in the photochemical reaction.

Data supporting that **Ruα** and **Ruβ** complexes are photocatalytically active for the same reaction in the presence of a sacrificial donors such triethyl-amine (TEA) are shown in **Figures 2.1.8** to **2.1.13**. For the photochemical reduction, all solutions were run in a quartz Schlenk cuvette which was thoroughly degassed with N_2 or with CO_2 gas prior to irradiation. The cuvette was inserted in a photoreactor with point source lights emitting at 470 nm ± 20 nm. The photon flux was 1 x 10^{-5} photons/second as measured by chemical actinometry. The progress of the photochemical reaction of **Ruα** and **Ruβ** was monitored by recording the respective electronic spectra at selected irradiation intervals.

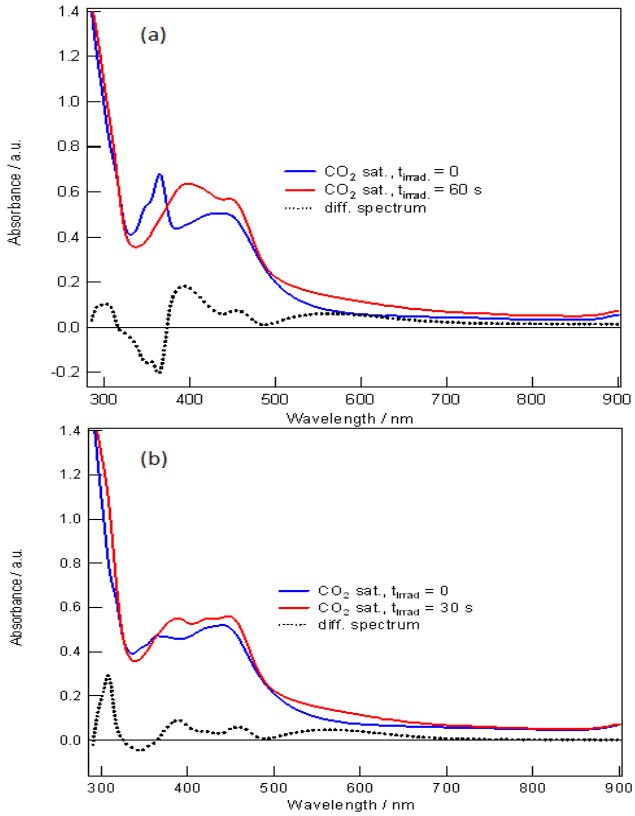

Figure 2.1.8 Comparison of the photochemical changes of **Ruα** (a) and **Ruβ** (b) in a CO_2 saturated DMF:H_2O solution: spectra before irradiation (blue solid line) and after irradiation (red solid line). Spectra in black dots correspond to the spectral difference, ΔA, between irradiated and dark conditions. Complex concentration = 22 μM in both cases and [TEA] = 0.25 M.

Figure 2.1.8 shows the absolute spectra of **Ruα** and **Ruβ** in a CO_2-saturated solution containing 0.25 M TEA (sacrificial donor) before and after visible light irradiation. This figure also contains for each complex the difference absorption spectra, ΔA, obtained by subtracting the initial from the final spectrum of each complex in order to emphasize changes that could be oversight in the respective absolute spectrum. The ΔA spectra contain bands pointing up, for the appearance of new species, whereas the opposite holds for bands

pointing down. The main features in the ΔA spectrum of both complexes is a broad band appearing in the 500-650 nm region accompanied by two sharper bands at 388 and 460 nm.

To determine the effect of CO_2 on the photochemical behavior of **Ruα** and **Ruβ,** the evolution of their individual ΔA spectra in DMF:H_2O during irradiation in N_2 and in CO_2 is compared in **Figures 2.1.9** and **2.1.10** respectively. Both figures show some similarities and essential disparities in their evolution in N_2 and CO_2 respectively. Thus, **Figure 2.1.9** compares the photochemistry of **Ruα** (2.2 x 10^{-4} M) under continuous irradiation in N_2 (**Figure 2.1.9** a) and CO_2 (**Figure 2.1.9** b) using 0.25 M TEA as a sacrificial donor. Arrows in each frame are indicating the time evolution of the corresponding spectral peaks. In the presence of N_2, the continuous photolysis brought about the bleaching of two sharp bands at 349 and 364 nm concurrent with the appearance of new species manifested in bands pointing up at 390, 460, 517 and 575 nm respectively; these bands reach a steady-state condition in ca. 400 s, with the highest contribution occurring at 517 nm. Of all these bands, those at ca. 390 and 460 nm are the most peculiar because they are the first to appear and they grow during the initial 150 s of irradiation, then their intensity goes down at the expense of other bands located at higher wavelengths (Figures **Figure 2.1.9** a and **Figure 2.1.11** a). For instance, the band at 575 nm is seen to continuously grow in a time window of 400 s while that at 517 nm appears after a certain delay (**Figure 2.1.11** a). The particular behavior of the bands at 390 and 460 nm seems to point out to formation of a species (likely a radical) than is then converted to another more stable species (detected at 517 nm).

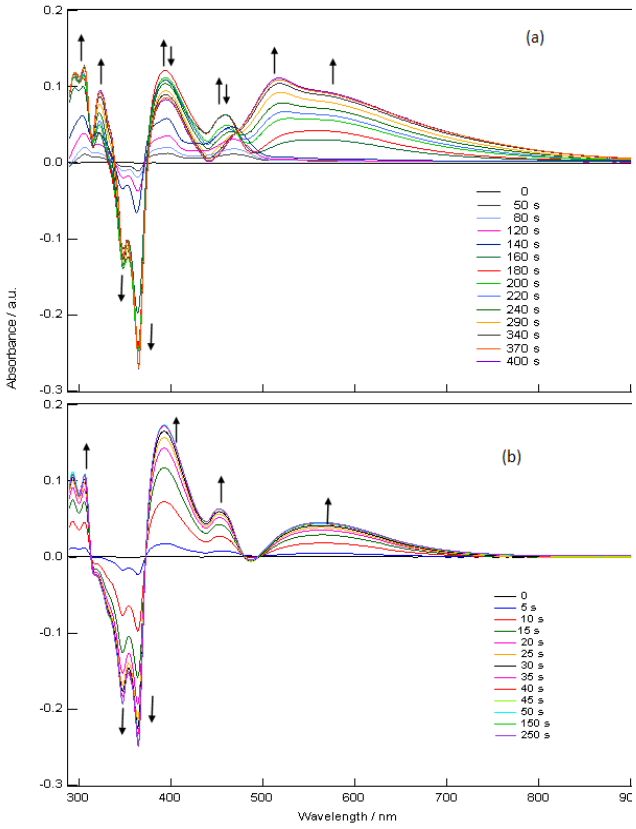

Figure 2.1.9 Selected Transient ΔA spectra of **Ruα** (2.2 x 10^{-4} M) during photolysis in N_2 (a) and in CO_2 (b) saturated DMF/TEA (0.25 M)/H_2O (1 M) solutions. Peaks pointing down indicate bands disappearing while those pointing up correspond to new bands appearing as a consequence of the photochemical reaction.

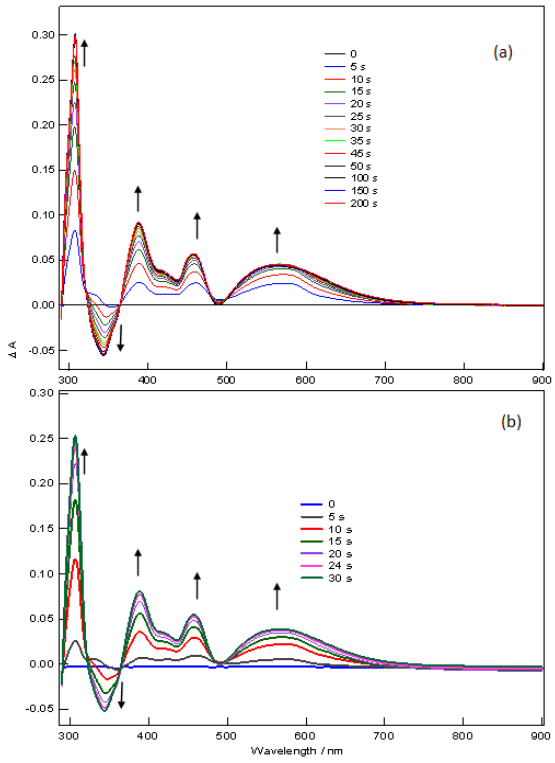

Figure 2.1.10 Selected transient ΔA spectra spectra of **Ruβ** (2.2 x 10^{-4} M) during photolysis in N_2 (a) and in CO_2 (b) saturated DMF/TEA (0.25 M)/H_2O (1 M) solutions.

spectral features attained with and without CO_2. The main changes observed are the bleaching of the 344-nm band (as characteristic of the initial complex concentration) counterbalanced with the growing of bands at 308, 388, 458 and 564 nm. The changes of the 344, 458 and 564 nm bands as a function of the irradiation time in N_2 are shown in **Figure 2.1.12**. The time to reach the steady-state spectral profile is slightly shorter in the presence of CO_2 (see **Figure 2.1.10**) getting there in 30 s vs. ca. 75 s in N_2-saturated media, i.e. ~ 2.5 times faster because of the presence of CO_2. These changes are consistent with a one-electron reduction of the complex, induced by a ^{1}MLCT excitation of the Ru π→ ptpbβ dπ band in the complex followed by reductive quenching of the ^{3}MLCT excited state by TEA to trap the electron on the ptpbβ ligand to

When the photolysis is measured in CO_2-saturated solutions, the avidity of the **Ruα** complex for carbon dioxide is clearly demonstrated in the short time to reach a steady-state spectrum, ca. 50 s (**Figure 2.1.1**b), about 6 times shorter than that for N_2-saturated DMF/TEA solutions. Moreover, the spectral contribution at 517 nm is clearly smaller in the presence of CO_2 with respect to that in N_2 while that at 460 did not show any decrease in CO_2 at variance with what is observed in a N_2-saturated solution.

Figure 2.1.10 compares the photochemistry of **Ruβ** (2.2 x 10^{-4} M) under continuous irradiation in N_2 (Fig. 6a) and CO_2 saturated (Fig. 6b) DMF solutions containing 0.25 M TEA as sacrificial donor. Contrasting with the effect of CO_2 in the photochemical spectral evolution of **Ruα,** the respective ΔA spectra of **Ruβ** showed very similar

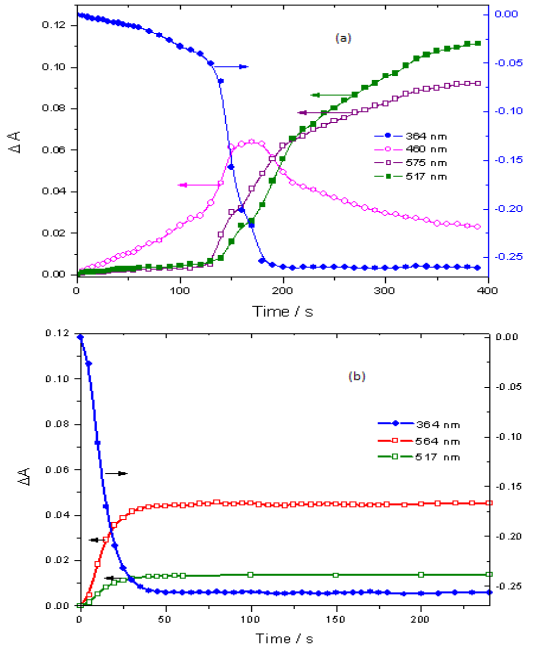

Figure 2.1.11 Photochemical evolution of selected bands of **Ruα** (2.2 x 10^{-4} M) in the absence (a) and in the presence of CO_2 (b). Data from Figure 2.1.9.

form $[(phen)_2Ru^{II}(ptpb\beta^{\bullet-})]^{+}$. This reduced complex is stable and can be re-oxidized to the starting complex $[(bpy)_2Ru(ptpb\beta)]^{2+}$ upon introduction of air.

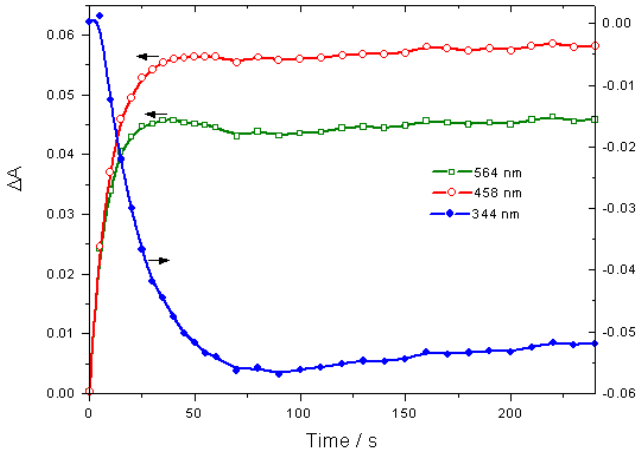

Figure 2.1.12 Photochemical evolution of selected bands during irradiation of **Ruβ** (2 x 10^{-4} M) in N_2-saturated DMF/TEA (0.25 M)/H_2O (1 M, pH 5.5). Data from Figure 2.1.10.

To attest the photocatalyst capability to continuously CO_2 reduction, serial experiments consisting in cycles of irradiation / dark periods (for CO_2 replenishing in the photochemical cell) were carried out. A representative experiment for complex **Ruβ** in a CO_2-saturated solution is shown in **Figure 2.1.13**. In this figure, there are three plots recorded during irradiation times of 30 s each separated by a 5 min dark periods in which CO_2 is bubbled to reestablish a saturation condition. Each photoreduction process required 30 s to be completed. During the irradiation times, the band at 564 nm senses the formation of the protonated monoreduced (**$Ru\beta^{\bullet-}$ → HRuβ)** species in DMF:H_2O, while the band at 344 nm is just indicating the disappearance of the initial **Ruβ** complex. It is worth noticing that the three irradiated periods showed very similar temporal profiles for both **HRuβ** and **Ruβ** species pointing to reversible photocatalyst regeneration.

Although $[(phen)_2Ru(dppz)]^{2+}$ appeared to be well–suited for generating a reduced pyridine functional group following the well-established photochemistry of ruthenium-polypyridyl family of coordination complexes, the electrochemistry data showed that **Ruα** and **Ruβ** are better candidates because of their less negative redox potentials compared to the $[(phen)_2Ru(dppz)]^{2+}$ and therefore they are better receptors for the photoexcited electron from the ruthenium moiety. Excitation of these complexes with visible light in the region of 400-500 nm forms an excited $MLCT_1$ state in which the pbtp (α, β) ligand is reduced by 1 electron in a similar way to dppz does. This excited state quickly relaxes to a second excited state, $MLCT_0$, in which the electron on the pbtp (α, β) ligand moves from a bpy-like orbital to a phenazine-like structure. Reductive quenching

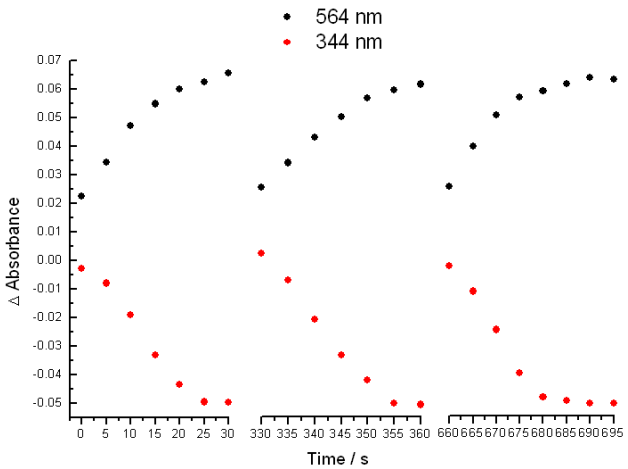

Figure 2.1.13 Three consecutive photocatalytic periods of **Ruβ** in CO_2 saturated DMF/TEA (0.25 M)/H_2O (1 M) solutions. The period of CO_2 bubbling gives rise to the removal of the reduced CO_2 species coordinated to the complex and thus releases the complex to work again in the next irradiated period.

of the Ru^{3+} center with sacrificial reductants traps this electron on the dppz ligand and thus 'photogenerate' an analogue of the pyridine radical.

*Spectroelectrochemical data were found extremely useful to clarify and differentiate the reaction pathways associated with the photocatalytic CO_2 reduction by **Ruα** and **Ruβ** complexes.* Thus, differential reflectance/potential curves are shown able to track **Ruα** and **Ruβ** electroreduced species which play key roles in the CO_2 photocatalytic conversion. These species are followed at selected wavelengths chosen from the photochemical data (**Figures 2.1.8 to 2.1.12**). Differential reflectance, δR/R, vs. potential profiles in N_2 and CO_2 saturated solutions are shown in **Figure 2.1.14**a for complex **Ruα** and in **Figure 2.1.14**b for **Ruβ** during a cyclic potential scan shown unfolded. The applied potential perturbation consisted in an ac signal (11 Hz, 50 mV_{p-p}) superimposed on a slow potential scan (2 mV/s). These δR/R /potential curves are shown at wavelengths of 575 and 564 nm to track the electrochemical formation of monoreduced monoprotonated H**Ruα** (formed by protonation of radical **Ruα**$^{\bullet-}$) and H**Ruβ** (from **Ruβ**$^{\bullet-}$) species respectively. The scan starts at 0 V to -1.0 V and then back to 0 V. The ordinate scale is such that the appearance of electrochemically generated species gives rise to positive δR/R signals, regardless of the direction of the scan (positive- or negative-going).

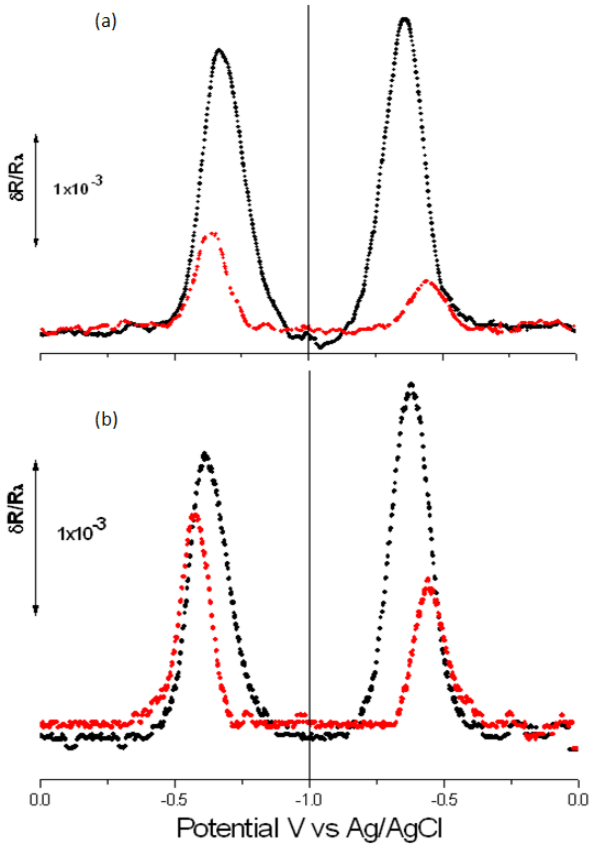

Figure 2.1.14 δR/R vs. potential curves of **Ruα** at 575 nm (a) and **Ruβ** at 564 nm (b) in DMF containing 0.1 M $TBAPF_6$. These runs were recorded as a function of potentials under N_2 (black trace) and in saturated CO_2 solutions (red trace). The working electrode was a mirror-polished Pt disc subjected to a sin potential wave (11 Hz, 50 mV_{p-p}) superimposed on a 2 mV/s potential scan.

First electroreduced and protonated species, H**Ruα** and H**Ruβ**, in N_2 saturated solutions shows sharp peaks on both the forward and reverse scans (**Figure 2.1.14**, black traces) reaching a maximum at -0.65 V and at -0.60 V respectively.. These optical peaks are corroborating that the reduced intermediate for **Ruα** is formed at more negative potentials than for **Ruβ**. More importantly, in both complexes the intensity of the signal during the reverse scan is higher than that on the forward sweep since a radical concentration build-up is occurring with time at the interface as expected in a diffusion controlled process.

Different profiles are obtained after CO_2 has been bubbled through the solution for at least 30 minutes (**Figure 2.1.14**, red traces). For both complexes the bands

intensities are significantly smaller indicating that the complex reduced intermediates, **Ruα**$^{\bullet-}$ and **Ruβ**$^{\bullet-}$ are being consumed by CO_2 according to a catalytic EC'-type mechanism described before, *vide supra.* Changes in intensity brought about by the presence of CO_2 are more drastic for **Ruα** than for **Ruβ**. Besides, for both complexes the maximum of the optical signal is smaller on the reverse scan than in the forward scan. This is at variance with their respective behavior in N_2 and is indicating that the CO_2 precludes the radical concentration build-up by chemically reacting with. Other important piece of information from the δR/R is that the amount of radical intermediate in the presence of CO_2 is significantly smaller for **Ruα** than is for **Ruβ** (as shown by the intensity of the optical signals in Figs **Figure 2.1.14**a and b). Two possibilities may give rise to this situation: i) CO_2 reacts faster with **Ruα** than with **Ruβ** and therefore less amount of the radical intermediate is spectroelectrochemically detected at the interface and/or ii) in the case of **Ruα**$^{\bullet-}$ the concentration available for modulation is even smaller than for **Ruβ**$^{\bullet-}$ because of the presence of a dimerization reaction consuming, in addition to CO_2, the radical species. The second situation seems more likely as it is supported by photochemical data and also by the CV runs in Figure 3 where complex **Ruβ** reaches a net plateau with higher current than that of **Ruα** which barely defines it. Therefore, the δR/R plots corroborate that **Ruβ** is not only energetically more favorable (lower negative potential) than **Ruα** but that it also reaches higher catalytic currents, and therefore higher efficiency for CO_2 conversion to its reduced products.

δR/R/potential curves for complex **Ruα** were also obtained at 517 nm to explain the photochemical mechanism in the absence and presence of CO_2. In the absence of CO_2, the species tracked at 517 nm is clearly seen to be formed in the same potential range than that at 575 nm (**Figure 2.1.15**). However, in the presence of CO_2, the signal at 517 nm practically disappears. Therefore, we are tentatively assigning the band at 517 nm in the reduction of **Ruα** in N_2 to the formation of a σ bonded dimer which amount is found significantly smaller than that of the monomer (red and black traces in **Figure 2.1.15**). Importantly, the dimer signal is significantly attenuated in the presence of CO_2 (blue trace in **Figure 2.1.15**) because of competition between the reaction of the H**Ruα** with CO_2 and the formation of a σ-dimer. This dimerization reaction seems not to occur with complex **Ruβ** as corroborated by no optical signal at 517 nm in the δR/R-potential trace either in absence or presence of CO_2.

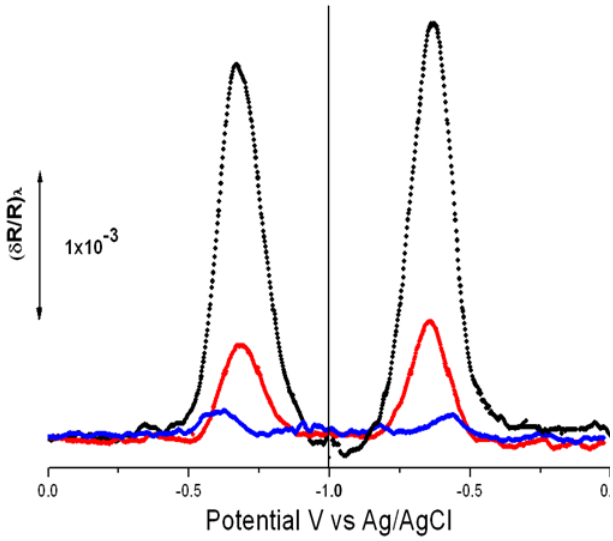

Figure 2.1.15 Comparison of δR/R vs. potential curves of **Ruα** at 517 nm in N_2 (red) and in CO_2 (blue) saturated DMF: H_2O solution containing 0.1 M $TBAPF_6$. For comparison, the trace at 575 (black) in N_2 is included. Other conditions are as in Figure 2.1.14.

We intended to quantify the photocatalytic activity of the existing system in the presence of AA or TEOA and then to replace these sacrificial donors with an electrode to so as to incorporate this CO_2 photoreduction chemistry into a photoelectrochemical cell (PEC). The key issue in such a PEC is the inability of the conducting electrode surface to directly reductively quench the photoexcited ruthenium complex. Due to the high density of states (DOS) at a metal surface, quenching of the photoexcited ruthenium complex generally occurs via energy-transfer (ET) quenching over reductive electron-transfer (eT) quenching. In order to lower the DOS, we are chemically modifying the electrode surface with redox-active molecular groups which we hope will reductively quench the chromophore and then act as a redox shuttle to the electrode surface. Metallic electrodes were found to quench the photoexcited states of the molecular chromophores by energy-transfer processes, resulting in the transiently stored energy being lost as heat. In order to determine the electron-transfer efficiency of a regular electrode as well as the product selectivity and yield, we examined the galvanostatic electrolysis of the ruthenium complex in the presence of the CO_2 substrate in DMF containing 1 M H_2O. The role of the electrode (reticulated vitreous carbon) is to provide a constant amount of electrons to the Ru complex in its first electroreduced state and thus prime the process for CO_2 conversion to liquid products.

In order to determine the electron-transfer efficiency of a regular electrode as well as the product selectivity and yield, we examined the galvanostatic electrolysis of **Ruβ** complex in the presence of the CO_2 substrate in DMF. The galvanostatic electrolysis was performed in a two compartment cell and at a constant current of -0.6 mA to force the reaction to occur at a constant rate. The chosen working electrode was a 4 cm height by 3.5 cm dia. reticulated vitreous carbon cylinder (a typical electrode for electrolysis and also for organic electrosynthesis due to its inert nature and high surface area) that has a platinum contact at its top end. The counter electrode was a 2 cm x 8 cm Pt foil place in a separated compartment where no ruthenium complex was present. The working electrode cell compartment contained 300 μM of the **Ruβ** complex in DMF:water (98:2) solution with 0.1 M $TBAPF_6$ as supporting electrolyte. The solution was saturated with CO_2 and the cell was kept pressurized and sealed.

The temporal evolution of the electrode potential profile recorded during a galvanostatic (controlled-current) electrolysis of **Ruβ** (300 μM) in CO_2-saturated a DMF:H_2O solution is shown in **Figure 2.1.16**. The working electrode was reticulated vitreous carbon and the role of the electrode is to provide a constant amount of electrons to the Ru complex in its first electroreduced state and thus prime the process for CO_2 conversion to liquid products.

The electrode potential is seen to stabilize at ca. -0.6 V (first electroreduction process of the complex) for a period of time spanning 6 hours and then the potential is seen to rapidly evolve to more negative values associated to the second electroreduction of the complex and remains there for at least 15 hours. The abrupt negatively potential shift at ca. 6 h electrolysis signals the end of the first electrocatalytic process. A coulometric calculation of the number of electrons consumed in the time period of the first plateau reveals that 5.5 equivalents of electrons per **Ruβ** were consumed during this electrolysis period (at -0.6 V). This value coincides fairly well with the number of electrons needed for each **Ruβ** to turnover 6 times to convert CO_2 to methanol.

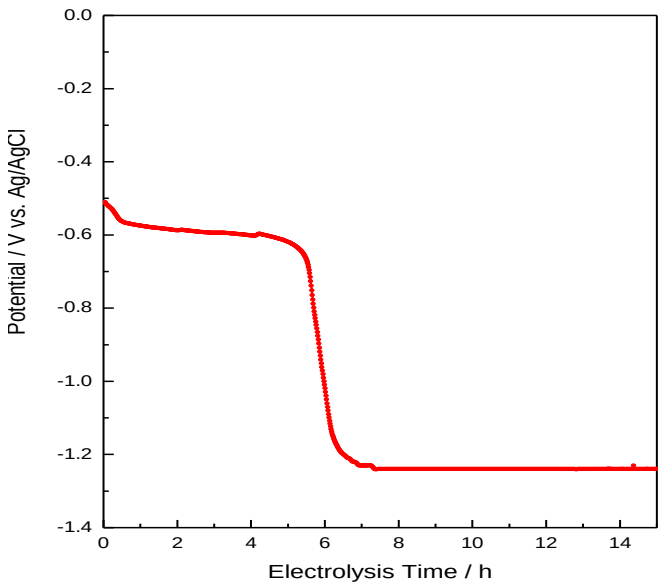

Figure 2.1.16 Potential/time profile recorded during cathodic galvanostatic electrolysis of **Ruβ** (300 μM) in DMF: H_2O (1M, pH 5.5) saturated with CO_2.

For product analysis, both the chromotropic colorimetric test (for HCOOH and HCOH) and GC-MS were performed on aliquots removed periodically during the electrolysis. Before performing product analyses, removal of the supporting electrolyte as well as the cationic ruthenium complex was achieved with Amberlite IRN-150 ion-exchange resin. After this treatment, the removal of the Ruthenium complex was revealed by the loss of coloration of the treated solutions. Then, the next reaction is that of the clear solution with 2N HCl (1 drop) and 80 mg Mg ribbon in a test tube immersed in an ice bath. Once there is no more gas evolving, the solution is removed from ice and 1.5 mL of chromotropic acid reagent (0.6 g in 200 mL conc. H_2SO_4) is added. The mixture is incubated at 60 C for 30 min and then centrifuged clear of white precipitate. The presence of formic acid and formaldehyde is evidenced by the generation of a violet solution with absorbance peaks at 482 and 584 nm. A calibration curve with solutions of known concentrations of formic acid was obtained in the range from 10-500 μM and used to analyze formic acid and formaldehyde in solutions of $[Ru(phen)_2pbtp\beta](PF_6)_2$ in DMF + 0.1 M TEA. For detection of methanol, also a colorimetric reagent (ceric ammonium nitrate) which is specific for alcohols was tested. Other carbon-containing product is CO and it was detected in minor amounts in the gas portion of preliminary photochemical runs by GC analysis with a Shin carbon column and a TCD detector.

By using the colorimetric test, frequently cited by others in the field for the detection for formaldehyde and formic acid by the chromotropic acid test, we detected both formate and formaldehyde in a 60:40 ratio at the end of the electrolysis (15 h). A semi-quantitative determination of the TON using absorbance measurements and a calibration curve revealed ~6 TON in this experiment. Formaldehyde was directly detected while formic acid was detected after an acid reduction procedure.

The biggest issue here is the difficulty in quantifying the MeOH produced as the solvent requirements make straightforward gas chromatographic (GC) analysis difficult. In order to retain the desired photophysical properties of the ruthenium chromophore for CO_2 reduction, we used a solvent system composed of DMF:water (98:2) or MeCN:water (98:2); i.e. the main solvent component is organic thus affording high CO_2 solubility and the relatively low amount of water provides the required protons to generate liquid photoreduced products (formic acid, formaldehyde, methanol). The presence of water in the organic media is required to provide protons to the reduced

products of CO_2. However, as the water concentration is increased, the lifetime of the photoexcited state of the Ru complexes diminishes to the point where the photocatalyst is inactive in 100% water. Unfortunately, GC analysis of the solvent gives a huge solvent peak (for both DMF and acetonitrile) which largely obscures the formic acid and methanol peaks. New GC columns and methodologies were explored to remove these obstacles and obtaining good quantitative data.

GC-MS using a non-polar capillary column was found appropriate for detecting formation of *methanol* after 4 and 6 hours of electrolysis, that is, after a time period where the methanol concentration had reached a significant built-up, keeping the potential at the value of the first electroreduction. A Shimadzu GC-MS-2010SE chromatograph with a MS QP2010 detector and a AOC-20S sampler was used. The chromatographic column was Shimadzu SHRX105MS (30-m length and 0.25-mm inner diameter, part # 220-94764-02) set at 45 °C. The MS detector was set at 250 °C, and helium was used as the carrier gas. Calibration curves for different methanol concentrations in water showed that the methanol peak eluded at 1.52 min with a corresponding m/z = 31. Headspace GC-MS analysis was also performed by heating the electrolysis aliquots at 75°C to avoid any solvent interference. Typical runs are shown in **Figure 2.1.17**a and b. MS detection was performed at m/z values of 31 (CH_2OH^+), 30 (H_2CO^+), 29 (HCO^+), 28 (CO^+), 15 (CH_3^+) and 45 ($COOH^+$) to track formation of CO, HCOOH, H_2COH and CH_3OH. For aliquots taken after 6 (Fig. 12b) and 12 hours (Fig. 12c) of electrolysis the main formed product was always methanol which was eluded at ca. 1.56 min and is clearly tracked at m/z = 31, although is also seen also in the lower intensity peaks at m/z 29, 15 and 30. Formaldehyde is seen at m/z 29 and 30 and was found as the second predominant product at 6 hours electrolysis. For samples taken after 12 hours of electrolysis, methanol build up is more than double than

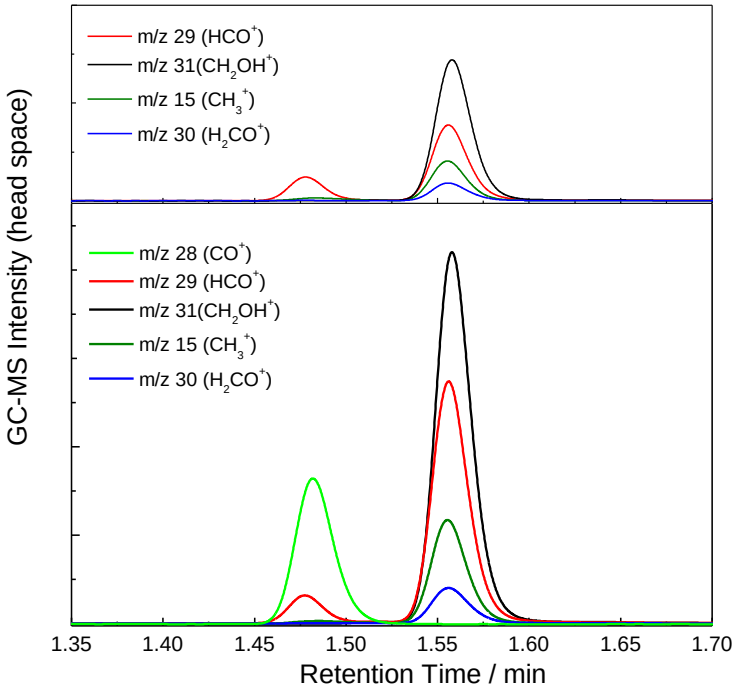

Figure 2.1.17 Head space GC-MS analyses of liquid aliquots removed after 6 h (a) and 14 h of electrolysis (b) respectively. MS peak intensities at 1.56 min (m/z = 31, 29, 15 and 30 from CH_3OH) increase ca. 2.5 times from 6 to 14 h of electrolysis. Formation of CO (m/z = 28, shown at 1.47 min, light green curve in (c)) is only present after the potential has evolved to ca. -1.2 V. Electrolysis conditions: 0.1 M $TBAPF_6$ (0.1 M) as supporting electrolyte; electrolysis working electrode = RVC cylindrical electrode; applied current = -0.6 mA.

at 6 hours and importantly, the product distribution changes after the potential evolves to ca. -1.2 V where the main product is still methanol, but the second dominant product was CO which was only formed at those more negative potentials. The **Ruβ** complex seems to still catalyze the CO_2 reduction at those negative potentials as indicated by the high currents depicted at -1.2 V (**Figure 2.1.7**). At these potentials the product distribution is: 70% of methanol, 22 % CO, 7 % HCOH and ca. 1 % HCOOH.

The jump to the more negative potentials of -1.2 V also suggests the end of 'normal' electrocatalysis, however a calculation of the number of electrons consumed by coulometry prior to this drop reveals that 5.5 equivalents of electrons per ruthenium entity were consumed during the initial electrolysis period (at -0.32 V). Interestingly, this value corresponds with the number of electrons needed for each $Ru(phen)_2pbtp\beta](PF_6)_2$ to turnover 6 times and thus convert CO_2 to methanol.

GC analysis with a ShinCarbon column and a TCD detector was used to analyze the gas portion of the electrolysis cell for formation of other carbon-containing products such as CO. These GC runs only showed CO_2 and a minor amount of air, corroborating that no CO was formed during the electrolysis.

The concentration of ruthenium complex in the cathode compartment was kept rather low (at 300 μM as higher limit) because higher concentrations were found less efficient because the enhancement of side reactions from the first reduced radical (either $Ru\beta^{\cdot-}$ or $Ru\alpha^{\cdot-}$) which is the catalytic entity that is needed to react with CO_2. The competition of side reactions, mainly σ-dimers, decreases the concentration of catalytic radical in solution in detriment of product generation from CO_2 reduction. It was also found that uα is more prone to form dimers than Ruβ although at present we do not have a clear mechanistic analysis of this topic.

Therefore, analytical techniques to quantify liquid and gaseous products formed during the galvanostatic electrolysis of $[Ru(phen)_2pbtp\beta](PF_6)_2$ as a homogeneous catalysts for CO_2 electroreduction under very low potential (-0.32 V vs. SHE) in the presence of interfering analytes such as DMF were optimized and as a consequence of it, formation of ***formic acid***, ***formaldehyde*** and ***methanol*** was detected. The chromotropic test seems a right choice for detection of formic acid and formaldehyde in the organic solvents while a non-polar capillary column appears to be the appropriate choice for GC detection of methanol in DMF:water solutions: the methanol peak shows up at 1.32 min while the solvent is not eluded from the column up to times longer than 6 min and therefore is not interfering with the product detection. Headspace GC analysis was the appropriate choice to avoid solvent interference. Besides, by headspace analyses it is possible to eliminate the treatment of the solutions with Amberlite IRN-150 ion-exchange resin which appeared to introduce artifacts into the analyte sample but was necessary in liquid analysis to selectively absorb all ionic species from the analyte sample.

Demonstrating that the same process can be driven photocatalytically has been a bigger challenge as the reaction mixture is more complex with the additional presence of a sacrificial donor. The quantitative methanol detection (GC-MS as described below) showed that addition of AA to the solution consistently gives a methanol product peak, even in control reactions. The cause of this methanol impurity was ultimately traced not to decomposition of the AA, but to the fact that AA is purified commercially via a methanol recrystallization step. Once the AA was properly cleaned, this problem

disappeared. Finally, a vapor transfer method to selectively remove all volatiles from the analyte and capture them in a liquid nitrogen cold trap was best option for detection.

With these problems in sample work-up and CH_3OH detection effectively solved, we then examined the complexes photocatalytic activity in homogeneous systems.

Hence, the following catalytic mechanism for the first photochemical and electrochemical reduction of **Ruα** is proposed as follows:

$$\textbf{Ru}\alpha + e^- \rightarrow \textbf{Ru}\alpha^{\bullet -} \quad \text{(the } \textbf{Ru}\alpha^{\bullet -} \text{ is detected at 460 nm)} \qquad (4)$$

$$\textbf{Ru}\alpha^{\bullet -} + H_3O^+ \rightarrow H\textbf{Ru}\alpha + H_2O \quad (H\textbf{Ru}\beta \text{ detected at 575 nm}) \qquad (5)$$

$$\textbf{Ru}\alpha^{\bullet -} + \textbf{Ru}\alpha \rightarrow \sigma\text{-dimer} \quad (\sigma\text{-dimer detected at 517 nm}) \qquad (6)$$

$$6\ H\textbf{Ru}\alpha + CO_2 \rightarrow 6\ \textbf{Ru}\alpha + CH_3OH + H_2O \qquad (7)$$

Radical formation by reaction (4) triggers competitive pathways (5) and (6) which are seen to counterbalance the initial growth of the 460 nm band at expense of those at 575 and 517 no respectively. It should be noted here, that the ruthenium catalyst was used in much lower amount that the substrate (CO_2) and its recovering is indicated by the arrow path joining reaction (7) with the reaction (4). Dimerization reaction (6) competes with protonation reaction (5) much more effectively in N_2- than in CO_2-saturated solutions because the protonated H**Ruα** species is expected to react with CO_2 to yield a radical carbamate intermediate (reaction (7)) similarly that in the case of pyridinium electrochemistry for the electrocatalytic reduction of CO_2.

For complex **Ruβ**, the photoreaction as well as the electrochemical reaction are not involving dimer formation, and a typical photocatalytic mechanism occurs for both the first and the second electron uptake at the pbtpβ distal and proximal orbitals:

$$\textbf{Ru}\beta + e^- \rightarrow \textbf{Ru}\beta^{\bullet -} \quad (\text{Ru}\beta^{\bullet -} \text{ detected at 460 nm}) \qquad (8)$$

$$\textbf{Ru}\beta^{\bullet -} + H_3O^+ \rightarrow \textbf{HRu}\beta + H_2O \quad (\text{HRu}\beta \text{ detected at 564 nm}) \qquad (9)$$

$$6\ H\textbf{Ru}\beta + CO_2 \rightarrow 6\ \textbf{Ru}\beta + CH_3OH + H_2O \qquad (10)$$

$$H\textbf{Ru}\beta + e^- \rightarrow H\textbf{Ru}\beta^- \qquad (11)$$

$$2\ H\textbf{Ru}\beta^- + 2\ CO_2 \rightarrow 2\ \textbf{Ru}\beta^{\bullet -} + CO + H_2O \qquad (12)$$

As reactions (8) and (9) proceed, the DMF:H_2O mixed solvent is undergoing proton depletion leading to a decrease in the rate to generate methanol. This assertion is supported by constant-current electrolysis data which at potentials of the first electroreduction peak was shown to generate methanol and other intermediates (formate and formaldehyde) but as the electrolysis time progresses, the potential

evolves toward the second electroreduction process which is able to mainly covert CO_2 to CO, i.e. without proton involvement.

From the electrochemical and photochemical data it can be extracted that **Ruβ** is a better catalyst for CO_2 reduction than **Ruα** mainly because: i) the lower unoccupied molecular orbital (LUMO) in the former lies at slightly lower energy (more positive potentials) than in the latter and ii) a competitive pathway originating after population of the LUMO in **Ruα** decreases its protonation capability and subsequent reaction with CO_2 (see reaction (6) competing with reactions (5) and (7)). In fact, the capability of **Ruα** to form a dimer (reaction (6)) easily than **Ruβ** seems to be rooted in that **Ruα** is more difficult to be protonated that its analogue complex and therefore reaction (5) is slower than reaction (6) and thus dimer formation is only seen for **Ruα** complex. By running CVs of both complexes in aqueous media as a function of pH, we have determined their pK_a values as 2.5 and 3.1 for **Ruα** and **Ruβ** respectively, therefore corroborating the easier protonation of **Ruβ** when compared to **Ruα.**

Figure 2.1.18 shows **Ruβ** as photocatalyst in a photochemical cycle involving reactions (5) - (7) for the CO_2 conversion to methanol. This scheme is purposely leaving aside the second reduction process of complex **Ruβ**. It only includes the $MLCT_1$ optical transition to the excited π_1^* level (~ 2.71 eV) of the complex, the internal electron transfer for the formation of the reduced phz-like intermediate, its protonation and formation of intermediates in which the CO_2 form an adduct with the pyridyl function of the ligand. The cyclic reaction also involved the reductive quenching of the photoexcited complex by triethylamine (TEA) sacrificial donor thus enhancing the photoconversion of CO_2 to methanol and/or intermediate products (such as formate and formaldehyde).

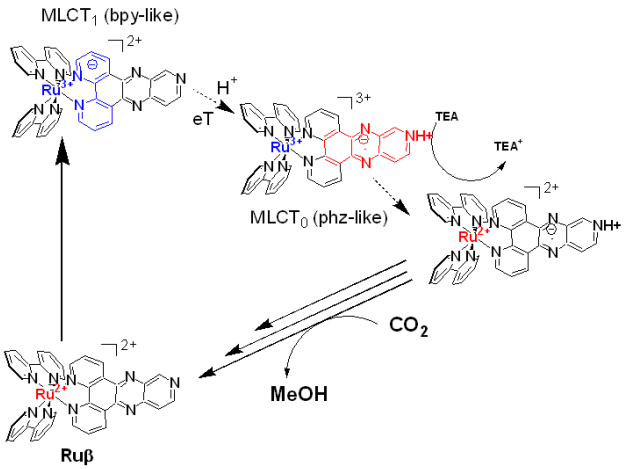

Figure 2.1.18 Photochemical cycle for excitation, internal electron transfer, protonation and reductive quenching of the complex Ruβ to reduce the CO_2 to methanol and/or intermediate products (such as formate and formaldehyde).

In conclusion both complexes **Ruα** and **Ruβ** are competent for photodriven CO_2 reduction in DMF solutions containing 1 M H_2O (pH 5.5) and leading to generation of methanol as the primary product. Each complex displays different mechanism although both of them showed fast, facile, and reversible one-electron reduction by electrochemical and photochemical methods. Electrocatalytic reduction of CO_2 occurs at the potential of the first electroreduction process for each respective complex (-0.57 V for **Ruβ** and -0.64 V for **Ruα**) but the reduction process in **Ruα** is complicated by a radical-anion dimerization side reaction which is fast in absence of CO_2 but that is partially cancelled in presence of CO_2.

Publications / Patents:

1. de Tacconi, N.R.; Chanmanee, W.; Dennis, B.H.; MacDonnell, F.M.; Boston, D.J.; Rajeshwar, K. **"Electrocatalytic Reduction of Carbon Dioxide Using Pt/C-TiO_2 Nanocomposite Cathode"** *Electrochemical and Solid-State Letters*, **2011**, *15 (1)*, B5-B8.
2. D. J. Boston, K-L. Huang, N. R. de Tacconi, F. M. MacDonnell and K. Rajeshwar, **Book chapter: Electro- and Photocatalytic Reduction of CO_2: The Homogeneous and Heterogeneous Worlds Collide?** in Photoelectrochemical Water Splitting: Challenges and New Perspectives **(**H-J. Lewerenz and L. M. Peter, eds.) RSC Press. In press.
3. D. J. Boston, C. Xu, D. W. Armstrong, and F. M. MacDonnell "**Homogeneous Photochemical Reduction of Carbon Dioxide to Methanol with Pyridinium Catalysts**" manuscript in preparation

2.2. Electro- and Photoelectrocatalytic Reduction of Carbon Dioxide

Preparation and Characterization of new Pt/C-TiO_2 and Pt-Pd/C-TiO_2 nano-composite electrocatalysts

Commercial carbon blacks (from Sid Richardson Carbon Co., Forth Worth) were used in the photocatalytic preparation of the Pt/C-TiO_2 or Pt-Pd/C-TiO_2 nanocomposite cathodes. The carbon black and TiO_2 (Degussa P-25) were mixed in a preselected ratio (95:5 or 90:10 %) and dispersed in deionized (DI) water (Corning Megapure) with the aid of an ultrasonic bath. The dispersion was then transferred to a 500 mL volumetric flask where 13.5 mL HCOOH (96%) and the required amount of metal salt precursor were added and then the total volume adjusted to 500 mL. The resultant slurry was transferred to the photoreactor and deoxygenated by N_2 bubbling.

The solution was irradiated for 30 min with a UV light source (450 W Model 66355 Xe arc lamp with f/1.0 condenser optics and power supply from Newport-Oriel) that was placed in the central annular compartment of a photoreactor and kept with constant N_2 bubbling to enhance the particle dispersion in the solution. This photocatalytic route for modifying a C-TiO_2 support with a noble metal (or bimetallic catalysts) hinges on the fact that the TiO_2 is a semiconductor and thus is capable of absorbing light of wavelengths equal to or greater than those corresponding to its energy bandgap, E_g (see **Fig. 2.2.1**). The photogenerated electron-hole pairs in the oxide, many of which escape recombination, diffuse to the particle surface where they

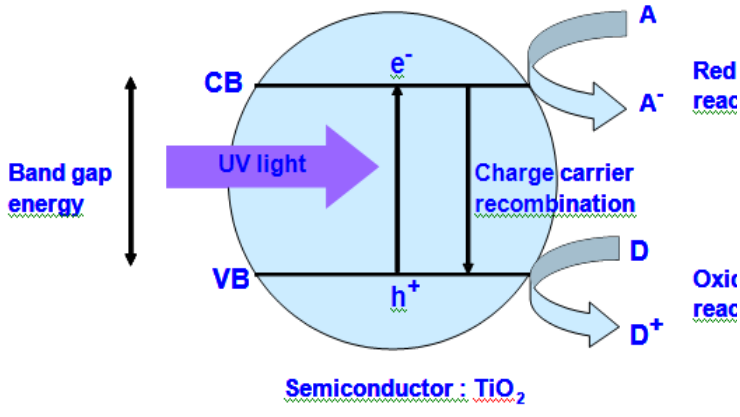

Figure 2.2.1. Schematic diagram of heterogeneous photo-catalytic process occurring in an illuminated semiconductor (TiO_2) nanoparticle. The photogenerated electron-hole pairs diffusing to the TiO2 surface are used to reduce an acceptor A

are available for useful reactions. The photo-generated electrons can be used to reduce a metal precursor species (e.g., $PtCl_6^{2-}$) to the elemental form.

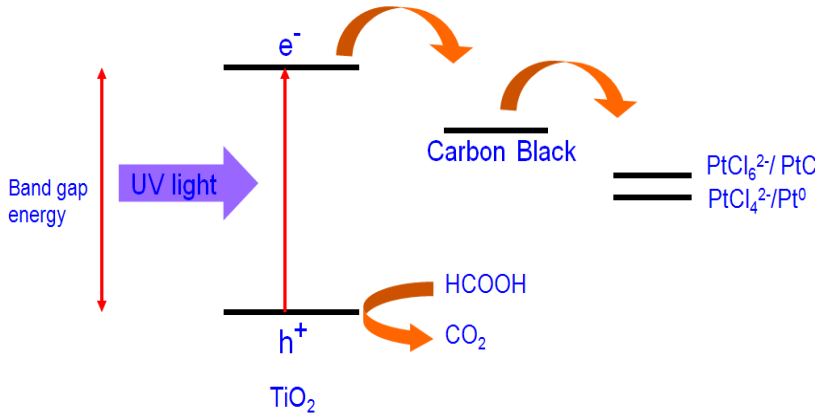

Figure 2.2.2. Schematic diagram of the transfer of photogenerated electrons from TiO_2 to carbon black electronic states leading to their delocalization and subsequent transfer to Pt(IV) species in solution.

A crucial finding in this study was that photo-induced electron transfer from the oxide semiconductor phase to the carbon black support results in uniform deposition of noble metal nanoparticles throughout the composite as a whole rather than being localized on the titania surface, thus supporting the transfer of photogenerated electrons from TiO_2 to carbon black electronic states leading to their delocalization and subsequent transfer to the soluble metal precursor to be deposited directly in the carbon black surface (**Figure 2.2.2**). This results in highly active noble metal photo-deposition on the C-TiO_2 composite support.

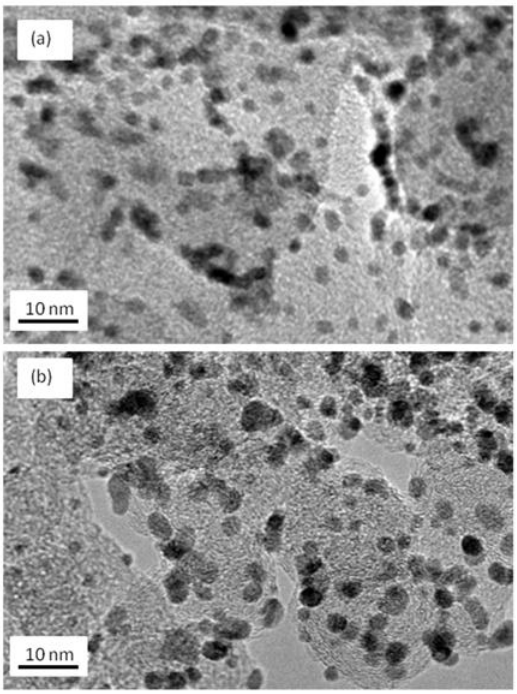

Figure 2.2.3. HR-TEM images of (a) Pt/C-TiO_2 and (b) Pd-Pt/C-TiO_2 nanocomposite surfaces.

The radiant output of the lamp was 192 mW/cm^2which implies a photon flux of 4.2 x 10^{17} photons/s.cm^2 over the 250-700 nm wavelength range. After completing the noble metal photodeposition, the resultant nano-composite powder was filtered, washed with deionized water, and dried overnight at 70°C. For preparation of bimetallic Pt-Pd/C-TiO_2, an essentially similar procedure was used except for addition of the Pd precursor salt to the photocatalytic deposition medium. The two metals (Pt and Pd) were photodeposited sequentially, first palladium and then platinum, with the total loading of the noble metal (50wt%) in the nanocomposite being maintained the same in both cases (35wt% Pd-15wt% Pt and 15wt %Pd- 35 wt% Pt).

Figure 2.2.3 contains high-resolution transmission electron micrographs of Pt/C-TiO_2 (**Fig. 2.2.3**a) and Pt-Pd C-TiO_2 (**Fig. 2.2.3**b) nanocomposite powders. In both images, the dark spots are the metallic nanoclusters that are seen

highly dispersed on the carbon-oxide support (showing corrugated appearance). Metal cluster sizes are seen to be in the range 3-5 nm with slighter larger sizes and elongated shapes in the case of the Pd-Pt nanocomposite (**Figure2.2.3b**). It is worth noting that a neat TiO_2 surface (i.e., without carbon black in electronic contact) affords Pt nanoparticles by photocatalytic deposition, that are significantly larger than those obtained with the C-TiO_2 support. In fact,**Figure 2.2.4** compares high resolution TEM images of platinum nanoparticles photodeposited on TiO_2 crystallites (**Figure 2.2.4** top) and on carbon black (**Figure 2.2.4**bottom). Observed in the HR-TEM image, that TiO_2 component appears as highly crystalline and as comparably large, transparent slabs while carbon black particles look as of corrugated morphology. In both cases, the metal deposition was instigated by TiO_2photoexcitation.

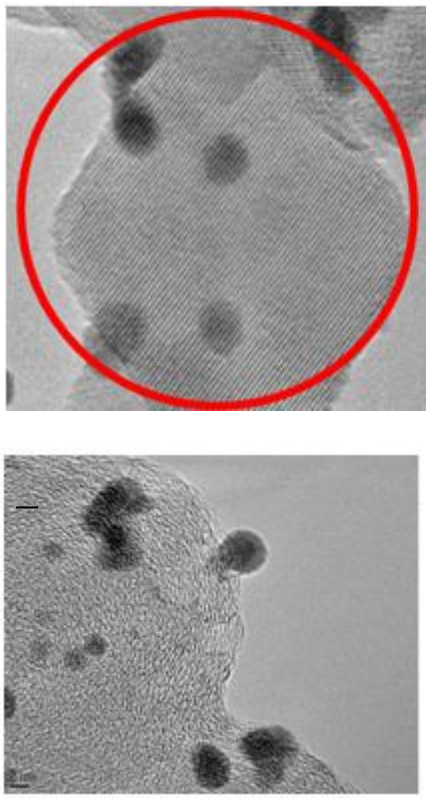

Figure 2.2.4 Comparison of Pt nanoparticles photodeposited on TiO_2 (top) and on carbon black (bottom) respectively. HR-TEM magnification was 2.5 higher in the bottom image. Bar size = 5 nm for top and 2 nm for bottom image respectively.

We have also performed XRD and XPS analyses. X-ray diffraction (XRD) patterns were obtained on a Siemens D-500 powder diffractometer using a Cu K_α source, and X-ray photoelectron spectroscopy (XPS) was performed on a Perkin Elmer/ Physical Electronics Model 5000C instrument. Thus, **Figure 2.2.5** contains representative XRD data for a Pt/C-TiO_2 sample compared with that for a Pt/TiO_2 sample (Pt/TiO_2) prepared except for omission of the carbon black in the dispersion. The Pt diffraction peaks overwhelm those from the TiO_2 component in the Pt/C-TiO_2 case (compared top and bottom XRD in **Figure 2.2.5**).

All the samples containing carbon were found to show the broad low angle fingerprint from the carbon black phase centered at a 2θ value of ~25°. The TiO_2 diffraction peaks are in excellent agreement with data reported in the literature. Average platinum particle size was estimated by Scherrer analyses performed on both the Pt (111) and (200) XRD peaks in the composite electrocatalysts as well as on the metal particles photodeposited on

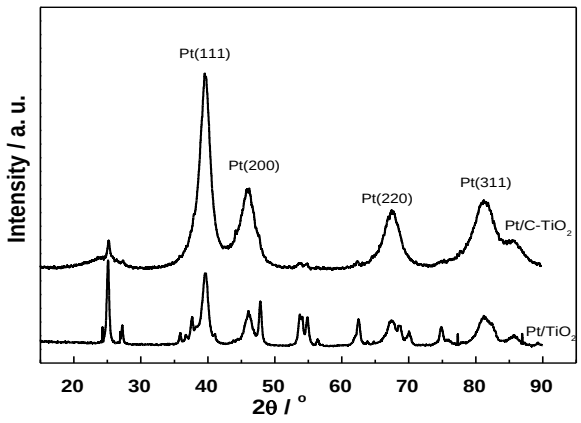

Figure 2.2.5 XRD patterns of Pt/C-TiO_2(50 wt% Pt) and Pt/TiO_2(5wt % Pt) nanocomposites.

TiO_2 nanocrystalline slabs. In agreement with the HR-TEM images (**Figure 2.2.4**), the platinum particle diameter was calculated as 4.7 ± 0.8 nm for the Pt/C-TiO_2samples while Pt photodeposited on TiO_2 resulted with an average metal diameter of 7.9 ± 0.8 nm. Importantly, Pt/C electrocatalyst prepared by chemical reduction showed a particle diameter almost double than the photocatalytically generated nanocomposite. Therefore, three trends emerged from these XRD data: (a) Photocatalytic deposition affords the finest Pt nanoparticle size which scales with the Pt loading in the composite electrocatalyst; (b) In the absence of carbon black, the Pt photodeposit nanoparticle size (on the TiO_2 surface) is significantly larger; and (c) Chemical deposition results in larger nanoparticle size of Pt than in the photocatalytic deposition case.

The electrochemically active surface area (ECA) is an important parameter in the characterization ofelectrocatalytic nanocomposites.The ECA can be calculated from CV data using the following equation:

$$ECA = \frac{Q_H}{[Pt]Q_C} \qquad (1)$$

where Q_H (mC/cm^2) is thecharge transferred under the hydrogen peaks involving 1 electron/platinum stoichiometry, [Pt] represents the Pt loading inthe working electrode and Q_C is the electrical charge associatedwith a monolayer adsorption of hydrogen on Pt (0.21 mC/cm^2). The CV traces (e.g., **Figure 2.2.6**) obtained different electrocatalysts were integrated to calculate the resulting ECA data. For determination of ECA, the electrocatalytic nanocomposite powders were deposited in the form of a thin film on glassy carbon (GC) disk electrodes. Coating was performed with 20 µL catalyst ink that was prepared as follows: 1 mg of catalyst was dispersed in 1 mL of water-isopropanol solution (80:20 volume ratio) with 10 min ultrasonication to create a uniform dispersion in the solvent. Then, 10 µL of 5 % Nafion® solution was added to the dispersion and additional ultrasonication was performed for 5 more min to have a well dispersed ink. Immediately after the final ultrasonication, 20 µL of ink was placed on the GC disk electrode (geometrical area = 0.196 cm^2) that was freshly polished with 0.1 µm alumina slurries and cleaned also by sonication in deionized water for 2 min, and completely dried. The ink on top of the GC electrode was allowed to dry at room temperature in N_2 atmosphere. The thickness of the resulting coated film, calculated through the Nafion® density, was in the range 0.05-0.08 µm.

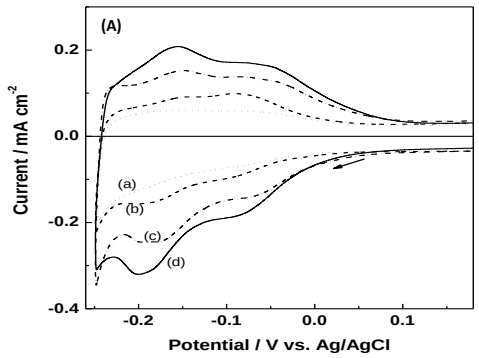

Figure 2.2.6 Comparison of the H adsorption/desorption voltammetric peaks for selected Pt/C-TiO_2 nanocomposites containing 5 (a), 10 (b) and 50 (c) wt % Pt. The three samples contained 5 wt % TiO_2. For reference a sample with 50 wt % and 10 wt % TiO_2 is also included (d). Pt SIDCAT 405 (a), SIDCAT 410 (b), SIDCAT 451(c) and SIDCAT 452 (d) at 20 mV/s in N_2 satd. 0.1 M $HClO_4$. (B) ECA as a function of platinum loading. For the ECA calculation, the Q_H is estimated by integration of the cathodic current/potential trace after subtracting the double-layer charge.

From the neat current/potential profiles encompassing the hydrogen electroadsorption (cathodic currents in **Figure 2.2.6**) and electrodesorption process (anodic currents in **Figure 2.2.6**) occurring on the platinum sites supported on C-TiO_2 support, it is therefore clear that the nanocomposite matrix is well percolated with a conductive carbon network to afford facile electron transport, and that it has high surface area which is ideally suited to support cascaded electron transfer beyond the $2e^-$ stage of an inert molecule such as CO_2.

Testing Pt/C-TiO_2 and Pt-Pd/C-TiO_2 nanocomposite electrocatalysts

To enhance electroreduction deeper than the $2e^-$ stage (to CO or formic/formate) as it would be required for any practical application, both on energetic grounds, and for avoiding problems associated with catalyst poisoning, we have used pyridinium as co-catalyst[3] which combined with the Pt/C-TiO_2 (or bimetallic Pt-Pd/C-TiO_2) nanocomposite cathode was found to provide a robust system for aqueous multi-electron, multi-proton reduction of CO_2 to alcohols.

Cyclic voltammetry (data not shown) of 0.2 M NaF solutions (pH: 5.4) containing 50 mM pyridinium cation (PyH^+) reveals the onset of the $1e^-$ reduction of the cation to the neutral pyridinium radical at ca -0.5 V on both Pt or Pd metal surfaces. Remarkably, an unmodified glassy carbon surface is completely inactive toward electroreduction of the pyridinium cation.

Rotating disk electrode (RDE) voltammetry measurements were performed in a glass electrochemical cell at room temperature using Pt/C-TiO_2 (or Pt-Pd/C-TiO_2) nanocomposite powders immobilized in the form of thin films on the glassy carbon RDE surface. A potential scan rate of 10 mV s^{-1} and a potential range from -0.2 V to -1.0 V were used. Blank runs with the same solution but saturated with N_2 instead of CO_2 were also performed. A platinum coil, placed in a separate compartment, served as the counterelectrode and a saturated Ag/AgCl/KCl electrode was used as the reference. All potentials below are quoted with respect to this reference electrode. The resulting datawas used to compare the performance of these materialsby analyzing the current/potential profiles recorded at pre-selected rotation speeds in a aqueous solution (pH ~5.4) of 10 mM pyridine saturated with CO_2. The acidity of the solution promotes the formation ofpyridinium cation (PyH^+).

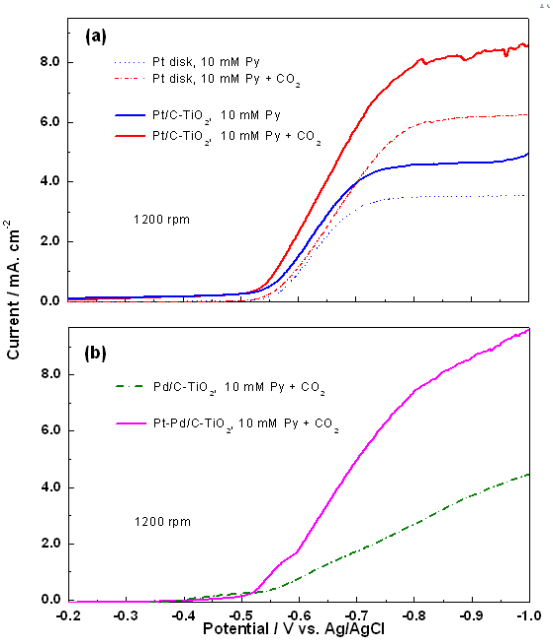

Figure 2.2.7 Comparison of hydrodynamic voltammograms of (a) a Pt/C-TiO_2 nano-composite RDE with a Pt RDE electrode and (b) a Pt-Pd/C-TiO_2 with a Pd/C-TiO_2 RDE respectively. The electrolyte was PyH^+-loaded NaF solutions saturated with N_2 or CO_2 as indicated in for each curve.

Hydrodynamic voltammograms (at ω

=1200 rpm) for a Pt/C-TiO_2 RDE and a polished Pt RDE (of same geometric area) in 10 mM pyridine-loaded NaF supporting electrolyte saturated with either N_2 or CO_2 are compared in **Figure 2.2.7**a.The Pt/C-TiO_2 nanocomposite contained 10 μg Pt dispersed on 0.196 cm^2 of the GC RDE surface whereas the Pt RDE translated to a Pt content of ca. 3-4 mg depending on the metal thickness. **Figure 2.2.7**b compares a Pt-Pd/C-TiO_2 (35wt% Pt - 15 wt% Pd) with a Pd/C-TiO_2 (35wt% Pd) in same CO_2 saturated solution conditions as in **Figure 2.2.7**a.

As seen in **Figure 2.2.7**a, addition of CO_2 leads to enhancement of cathodic current for both cathode materials, attesting to the catalytic role played by both Pt and the pyridine (Py) co-catalyst toward CO_2 reduction. The protonated PyH^+ is known to catalyzed the reduction of CO_2 to various products and at low overpotential. An EC'-type mechanism was demonstrated on platinum electrodes (E. Barton-Cole, P. S. Lakkaraju, D. M. Rampulla, A. J. Morris, E. Abelev, and A. B. Bocarsly, *J. Am. Chem. Soc.***132**, 11539 (2010)). More germane to the focus of this study, however, is the drastic (ca. 30% enhancement in cathodic current flow for the Pt/C-TiO_2 nanocomposite relative to the massive Pt electrode case (**Figure 2.2.7**a). This occurs in spite of the fact that the loading of Pt in the Pt/C-TiO_2 electrode is approximately a *million-fold* less than that corresponding to a Pt RDE. Thus the mass activity of Pt/C-TiO_2 as expressed by the current density normalized by the mass of platinum at -0.55 V are 46.4 and 76.6 $mA.mg^{-1}$ in N_2 and CO_2 respectively, whereas for the Pt disk (assuming ~ 1 g of metal content) the corresponding values are 1.44×10^{-4} and 2.51×10^{-4} $mA.mg^{-1}$ respectively. Significantly enough, close examination of the hydrodynamic voltammogram in the plateau region in **Figure2.2.7**a for the Pt/C-TiO_2 case in the presence of CO_2, shows noise that is consistent with the visual observation of gas bubbles on the electrode surface (attributed to adsorption of the CO_2 on the carbon black component of the nanocomposite). Comparable data trends were seen in the Pt-Pd/C-TiO_2 case (**Figure2.2.7**b). The adsorption of CO_2 on carbon surfaces, such as carbon black, graphite, activated carbons, carbon nanotubes and even graphene sheets, is well documented in the literature (V. Y. Gavrilov, and R. S. Zakharov, *Kinetics and Catalysis***51**, 609 (2010)) and seems to be the right combination with the metal sites for the outstanding performance of the nanocomposites when compare to that of bulk metal electrodes.

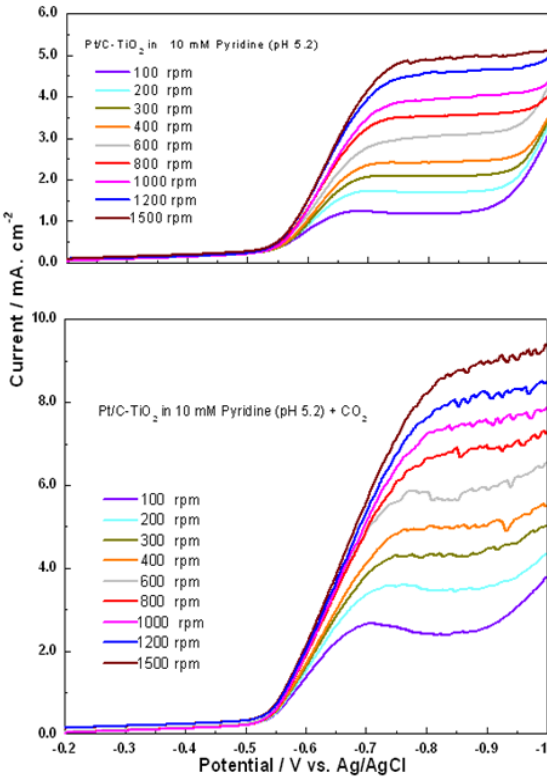

Figure 2.2.8 Hydrodynamicvoltammetry data for a Pt/C-TiO_2 RDE in 10 mM PyH^+ -loaded aqueous solutions (NaF, pH 5.4) saturated with N_2 (top) and CO_2 (bottom) respectively.

The hydrodynamic voltammetry trends, shown in **Figure2.2.7**a, were further elaborated for Pt/C-TiO_2 using variable rotation rates (**Figure 2.2.8)**. The cathodic current enhancement is seen at all ω and noise in the plateau region is unmistakable

when CO_2 is present in the electrolyte (compare **Figures2.2.8a and b**). The increase in current flow observed at potentials more negative than - 0.9 V in **Figure2.2.8** is associated with proton reduction (and hydrogen evolution). This process is not germane to this study and was not considered further.

Figure 2.2.9contains Levich plots (constructed from the hydrodynamic voltammetry data in **Figure2.2.8**) of the limiting current density, j_L vs the square root of the electrode rotation speed for the Pt/C-TiO_2 nanocomposite cathode in N_2 and CO_2 saturated solutions:

$$j_L = 0.62nFD^{2/3}\nu^{-1/6}C\omega^{1/2} \qquad (2)$$

In equation (2), *n* is the number of electrons transferred, *F* is the Faraday's constant, *D* is the diffusion coefficient of the electroactive species (PyH^+), υ is the kinematic viscosity of the electrolyte (~ 0.01 cm^2 s^{-1})[9], *C*is the PyH^+ concentration (mol/cm^3) at the respective solution pH and ω is the electrode rotation rate in radians s^{-1}. The values used for *D* and *C* were 7.6 x 10^{-6} cm^2 s^{-1} and 0.8 x 10^{-5} mol cm^{-3} respectively.

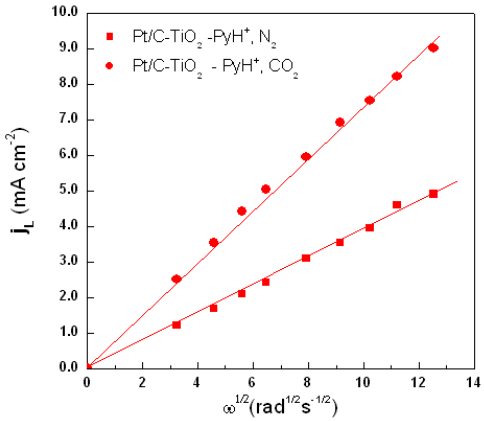

Figure 2.2.9 Comparison ofLevich plots for the electroreduction of PyH^+ in N_2 and CO_2 saturated solutions using a Pt/C-TiO_2 RDE. Slopes and correlation coefficients from least-squares fits are 0.401 $mAcm^{-2}$ $s^{1/2}$and 0.9986 and 0.718 $mAcm^{-2}s^{1/2}$and 0.9987 for the N_2- and CO_2 saturated solutions respectively.

A plot of j_L vs. $\omega^{1/2}$(Levich plot) should be linear for diffusion-controlled electrochemical processes. Both sets of data in **Figure 2.2.9** show good linearity; the slopes of the two Levich plots afford values for the electron stoichiometry (*n*) which are very close to 1.0 and 1.8 in N_2 and CO_2 saturated solutions respectively. Clearly, the pyridinium-catalyzed CO_2 reduction is sustained by the initial diffusion-controlled one-electron reduction of PyH^+ to $PyH^\bullet$ radical on Pt/C-TiO_2. Importantly, the nanocomposite electrocatalyst layer is thin enough (0.05-0.08 µm range) to not contribute to film diffusion-limited behavior.

Best performance was found with Pt/C-TiO_2 (50 wt% Pt, 5 wt% TiO_2)followed by the bimetallic Pt-Pd/C-TiO_2 (35 wt% Pt - 15 wt% Pd). Much lower currents were obtained with the Pd/C-TiO_2 (50 wt% Pd); thus indicating the importance of Pt nanoparticles in the composite for its superior performance. Importantly, the fine dispersion of the metal electrocatalyst on the carbon black and TiO_2components enhances significantly the efficiency of CO_2 electroreduction current relative to a neat Pt cathode under otherwise comparable reaction conditions. We rationalize that the enhancement is on one side because carbon black is acting as CO_2 absorbent thus concentrating its amount at the electrode interface and on the other side because TiO_2 enhances the fine dispersion of photodeposited metal nanoparticles.

Detecting products formed by dark CO_2 reduction on Pt/C-TiO_2 nanocomposite cathodes

For analyzing the CO_2 electroreduction products, galvanostatic polarization experiments were conducted in a two-compartment glass electrochemical cell to separate the anode and cathode reactions. The nanocomposite powder was immobilized as a thin film on extruded graphite electrode surfaces using the procedure

described above. The electrocatalyst loading on the graphite electrode (geometrical area 20.20 cm^2) was controlled at 0.25 mg/cm^2. The film electrode was then galvanostatically tested by imposing a cathodic current density 0.02 mA/cm^2 in 0.5 M KCl as supporting electrolyte and 10 mM of pyridine. The pH of solution was 4.5-4.8 (adjusted with 1M H_2SO_4). Before and during all electrolyses, CO_2 was continuously bubbled through the electrolyte to deoxygenate it.

Controlled-current electrolysis in a sealed two-compartment electrochemical cell containing large area Pt/C-TiO_2or Pt-Pd/C-TiO_2cathodes in contact with a CO_2 saturated aqueous solution was used to determine the stability of the prepared nanocomposites and to characterize the product speciation.

The stability of the nanocomposite electrodes were confirmed by recording the electrode potential during the 50-hour galvanostatic electrolyses and only a minor progressive potential drift (from -0.50 V to -0.58 V) was observed and thus attesting the good stability of the nanocomposite material. As the solution was purposely no buffered to avoid interference in the alcohols detection, this small potential drift is likely manifesting a progressive increase of pH as a function of time due to consumption of protons associated to products generation. No formation of H_2 was observed during the electrolyses as the chosen low current density promotes the electroreduction of pyridinium and subsequent catalytic conversion of CO_2 to alcohols through an EC'-type mechanism.

The electrolysis products were analyzed on a gas chromatograph (Model SRI 8610C equipped with a 1 m HayeSep DB column and FID detector, Restek Chromatography Products). Typical GC conditions used N_2 as the carrier gas at a flow rate of 20 mL/min. The injection port was at 200 °C and the column kept at 120 °C. After removal of the supporting electrolyte salt with Amberlite IRN-150 ion-exchange resin, sample aliquots from the galvanostatic runs were subjected to GC assays.

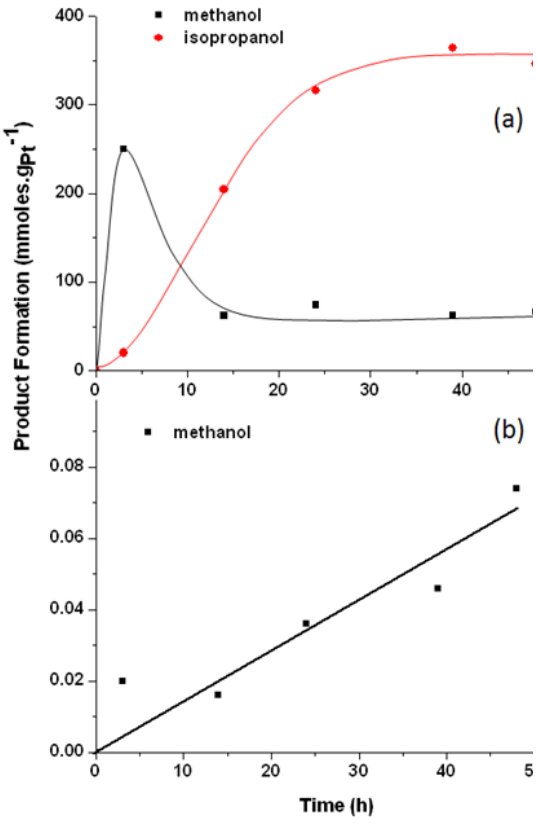

Figure 2.2.10 GC analyses as a function of time for constant-current electrolysis of CO_2-saturated solutions using: (a) Pt/C-TiO_2 and (b) Pt foil cathodes. Electrolysis conditions specified in the text.

GC analyses of the electrolysis solution revealed the formation of both methanol and isopropanol as solution products at the Pt/C-TiO_2 nanocomposite cathode (Fig. 2.2.10a). As shown in **Figure2.2.10**a, at short reaction times (t < 1h) methanol is the major product with lesser amounts of isopropanol. Subsequently, the amount of methanol drops precipitously whereas the isopropanol content increases regularly. We attribute this drop in methanol content to volatilization and entrainment of methanol in

the CO_2 stream (due to constant CO_2 bubbling). This is less of an issue with isopropanol due to its higher vapor pressure, and as seen in **Figure2.2.10**a, the concentration of isopropanol increases regularly up to 40 h after which production is flat throughout the electrolysis.Methanol and isopropanol were corroborated by co-injection with authentic samples and quantified by peak area integration using calibrations.

Only methanol was seen as the CO_2 electroreduction product in the Pt foil case (**Figure2.2.10**b). *Importantly, no CO was seen in the reduction products.* This is especially significant in that metals such as Pt or Pd are known to selectively produce CO on electroreduction of CO_2; clearly, the nanocomposite matrix facilitates deeper reduction (to alcohols) beyond the $2e^-$ CO stage. The mechanistic factors underlying this trend will be further probed in follow-on work that is planned.

Finally, we note that the production of alcohol per unit mass of Pt for the nanocomposite matrix case (**Figure2.2.1**0a) is *three orders of magnitude* larger than the Pt foil case (**Figure2.2.10**b). This represents substantial reduction in Pt and is an important advance toward improving the economics of electrochemical reduction of CO_2 to liquid fuels.

As a last remark, we want to emphasize that this work showed for the first time that nanocomposite cathode matrices derived from either Pt/C-TiO_2 or Pt-Pd/C-TiO_2 are effective electrocatalysts for aqueous CO_2 reduction in the presence of a solution co-catalyst such as the pyrdinium cation. The Pt/C-TiO_2 with 50 wt% Pt, 5 wt% TiO_2 is the optimized material in which the electrochemical conversion of CO_2 to alcohols was demonstrated. The use of pyridinium cation (PyH^+) as a solution co-catalyst is required to drive the reaction towards alcohols instead of formation of CO when the co-catalyst is absent. All these results are included in a recently published paper in *Electrochemical and Solid-State Letters*(*see Publication # 1 below).*

Demonstrate the viability of selected metal-loaded semiconductor nano-structures: Development of heterogeneous photocatalysts capable of photoreducing CO_2 using solar energy.

The use of inorganic semiconductors to photoreduce CO_2 to useful energy-rich products such as methanol is not a new concept and dates back to the 1970s. However, the quantum developments in materials nanotechnology and new semiconductor compounds that have taken place particularly during the past decade, prompted us to re-examine the viability of this concept. To prepare semiconductor nanoparticles and use them as photocatalysts, we used a solution combustion synthesis procedure which has to be optimized for each particular material. Three different semiconductor materials were chosen, namely $BiVO_4$, Bi_2WO_6 and $AgBiWO_8$, all with respective band-gap in the visible spectral region paving the way to efficient utilization of the solar spectrum. All three materials were examined for their photocatalytic activity in both photoreduction and photooxidation processes.

Three semiconductor nanooarticulate materials namely$BiVO_4$, Bi_2WO_6 and $AgBiW_2O_8$were prepared by solution combustion synthesis (SCS). The synthesis variables (selection of precursors, fuels, and post-annealing temperature) were optimized for best performance under light irradiation of the resulting nanoparticles. In

this way, we seek to control the important materials properties for photoactivity under visible light in the absence and presence of CO_2.

Solution combustion synthesis is both energy- and time-efficient. The exothermicity of the combustion reaction provides the energy requirement for the synthesis and the high reaction temperatures result in finely dispersed and porous morphology for the binary ($BiVO_4$ and Bi_2WO_6) and ternary ($AgBiW_2O_8$)oxide products (**Figure 2.2.11**). The effect of a post-annealing temperature was also analyzed in its effect on the crystallinity of the compound and particle size.

Figure 2.2.11. Appearance of the $BiVO_4$ (a), Bi_2WO_6 (b) and $AgBiW_2O_8$ (c) samples prepared by SCS and using urea as fuel.

Other advantages of SCS for the preparation are: a) simple homogeneous reaction involving just the dissolved precursors' salts and a fuel, both in water (see: Rajeshwar, K.; de Tacconi N. R. *Chem. Soc. Rev.***2009**, *38*, 1984) and b) incorporation of multiple components as co-catalysts.

The synthesized powders were characterized by transmission electron microscopy, thermal analyses, diffuse reflectance UV-visible spectroscopy, X-ray diffraction, surface area measurements, and X-ray photoelectron spectroscopy.

Analysis of UV-visible reflectance spectra of the SCS-derived powders using the Kubelka-Munk methodology affords values for the energy band-gap of 2.2 eV for $BiVO_4$, 2.7 eV for $AgBiW_2O_8$and 2.8 eV forBi_2WO_6 respectively. Clearly, $BiVO_4$ is superior (relative to the other two) in terms of better overlap with the solar spectrum. However when the three materials were compared in its photocatalytic activity, the better match with solar light is not the only variable determining the photoconversion performance.

To exemplify the difference between the particle sizes obtained by SCS and the most common solid state reaction (SSR), representative HR-TEM images of SCS-$AgBiW_2O_8$are compared with same compound prepared by SSR in **Figure 2.2.12.** The HRTEM images of SCS-$AgBiW_2O_8$depict both individual spherical nanoparticles with a mean average size of 6.6±1.0 nm (**Figure2.2.12A**), which are in accord with the particle size calculated by the Scherrer equation, and small aggregates (**Figure2.2.12B**) as a result of partial sintering occurring during the combustion synthesis process. Besides, EDX analysis of a SCS sample (**Figure2.2.12B**, inset) corroborates that the nanoparticles contain Ag, Bi, W and O with stoichiometric ratios as expected for $AgBiW_2O_8$.

It is worth noting that even without a post-synthesis thermal anneal step, partially crystalline samples were obtained from solution combustion synthesis which underlines the advantage with this synthesis approach from an energy input perspective to add to its high time efficiency as noted above. The SSR-$AgBiW_2O_8$ showed much larger particles and required 18 hours at 800°C in the preparation. This comparison vastly demonstrates the beneficial use of SCS as method to rapidly prepare uniform and smaller nanoparticles. Consistently with the smaller particle size, the SCS samples also have a significantly higher surface area ($35 m^2.g^{-1}$) relative to the SSR counterpart ($0.50 m^2.g^{-1}$).

When the SCS-derived semiconductor nanoparticles were compared in their photocatalytic activity, clear trends appeared. SCS-$BiVO_4$ showed excellent photocatalytic performance for dye oxidation but did not perform well as photocatalyst for reduction of CO_2. The contrasting behavior for photooxidation and photoreduction reactions seems to be rooted in that the energy of the $BiVO_4$ conduction band (CB) is rather low (even lower than the requirement for solar hydrogen generation) and likewise the driving force for photoreduction of CO_2 to useful fuels (CH_4 and alcohols) was found very limited.

Although Bi_2WO_6 and $BiVO_4$ are members of the Aurivillius family, they differ in that the conduction band of the first material is located at more negative potentials thanthe second although with the caveat that its energy band gap is 0.4 eV higher (2.8 eV vs. 2.4 eV in its $BiVO_4$ analog (vide supra). Both nanoparticulate semiconductormaterials, once optimized in the respective combustion synthesis, were found to have good photocatalytic performance for photooxidation reactions but behaving poorly for photoreductions reactions (i.e., CO_2 photoreduction and H_2 photogenetration).

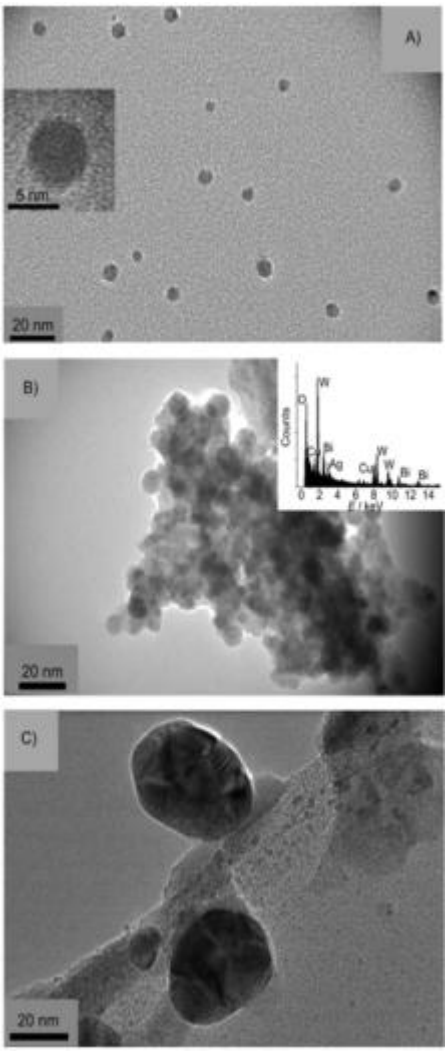

Figure 2.2.12 – HR-TEM images for SCS-$AgBiW_2O_8$ (A and B), and by SSR (C). Individual nano-particles (A) were also found as small aggregates (B). EDX analysis corroborates the material purity as the only extra element detected is Cu from the supporting mesh(insert in Figure 2.2.12B).

The ternary SCS-$AgBiW_2O_8$ was found to be the best of the three materials because of its high performance for both photooxidation and photoreduction reactions. A comparison of its photocatalytic activity for an oxidation reaction (specifically the methyl orange photodegradation) relative to that of $BiVO_4$ is presented in **Figure 2.2.13.** Clearly, the SCS-$AgBiW_2O_8$ nanoparticles outperform those of SCS-$BiVO_4$ in terms of proclivity to photochemically break down methyl orange in spite of the much lower overlap of the solar spectrum of $AgBiW_2O_8$ material.

The photocatalysis data in **Figure 2.2.13** were well fit by pseudo-first order kinetics in agreement with what is expected for methyl orange phocatalytic oxidation. The better performance of the ternary oxide is also clear in the comparison of the dye half-time is 3.61 h for $BiVO_4$ and only 1.13 h for $AgBiW_2O_8$. These comparative data underline a crucial fact: *The optical attributes only offer a partial glimpse into the suitability of a given photocatalyst for solar energy conversion or environmental remediation application.* These results are included in a recently published paper in the Journal of Nano Research (*see Publication # 2 below).*

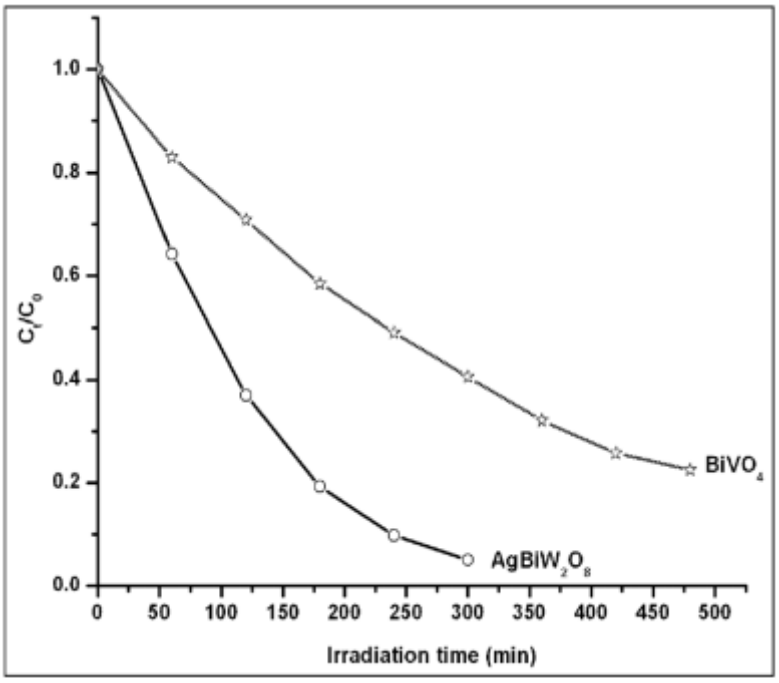

Figure 2.2.13 – Comparison of the photocatalytic activity of combustions synthesized $BiVO_4$ and $AgBiW_2O_8$ for the photodegradation of methyl orange.

In relation to the photo-reduction processes, the SCS-$AgBiW_2O_8$samples were metal-loaded with Pt nano-particles. In fact, it was found that $AgBiW_2O_8$modified with 1 wt.% Ptwere the best of all for both photooxidation and photoreduction reactions. The resulting performance for Pt-modified $AgBiW_2O_8$ in photoreduction reaction is presented next.

Photogeneration of Syngas and Methane on Pt-Modified $AgBiW_2O_8$

Syngas(or “synthetic gas”) is the name given to a gas mixture that contains varying amounts of CO and H_2gases. Common examples of producing syngas include the steam reforming of methane or liquid hydrocarbons, and the gasification of coal or biomass. Thermally mild (i.e., low temperature) alternatives for producing thistransportable chemical fuel mixture is obviously very significant from an energy perspective. Value is even further if the production process can be driven via a renewable solar energy source from a source greenhouse gas material such as CO_2.

Figure 2.2.14shows an energy diagram containing the band edges for $AgBiW_2O_8$ (band-gap = 2.7 eV) together those for $BiVO_4$ and Bi_2WO_6. Relevant solution redox levels such as those for water and CO_2 reduction as well as oxidation of water to O_2 are also included. Of the three semiconductors, the $AgBiW_2O_8$ showed the best driving force for photogenerated electrons to be used in CO_2 photoreduction and also hydrogen photogeneration under visible light.

SCS-$AgBiW_2O_8$ samples were modified with 1 mass % Pt islands using a photocatalytic procedure. The surface metal islands were used to enhance electron-hole separation during photocatalytic processes.

Figure2.2.15 contains the high-resolution XPS data for a SCS-$AgBiW_2O_8$sample in the binding energy regimes 3d for Ag (frame '**a**'), 4f for Bi and W (**b** and **c**), and 1s for O (**d**)] characteristic of the four elements in the compound. The Pt 4f signals for the Pt-modified $AgBiW_2O_8$ nanoparticles are depicted in **Figure 2.2.15e**. The XPS signals for the metal components are split due to spin-orbit coupling. The signals are located at 387.9 eV for silver (Ag $3d_{5/2}$), at 158.9 eV for bismuth (Bi $4f_{5/2}$) and at 35.1 eV for tungsten (W $4f_{7/2}$) respectively. These respective peaks for Ag, Bi and W are associated with Ag^+ or Ag^{2+}

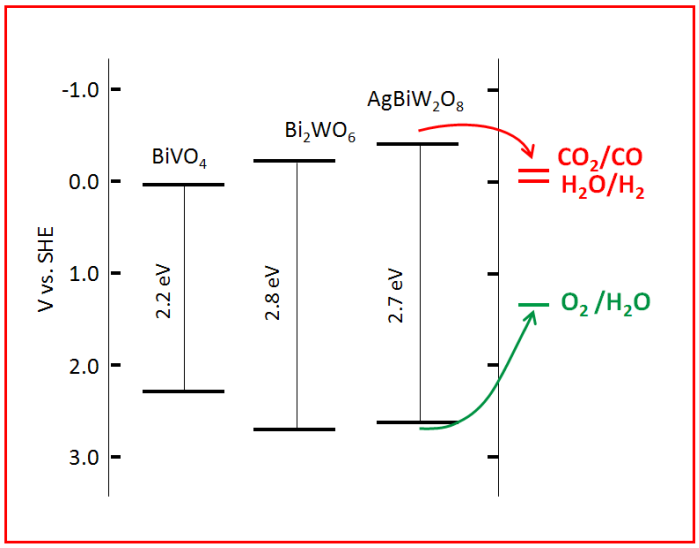

Figure 2.2.14. Energy diagram containing the position of the band edges (in a SHE potential scale) for the $AgBiW_2O_8$ semiconductor and the redox potentials for conversion of water to hydrogen, CO_2 to CO, and water to oxygen. The respective band edges for Bi_2WO_6 and $BiVO_4$ are included for comparison.

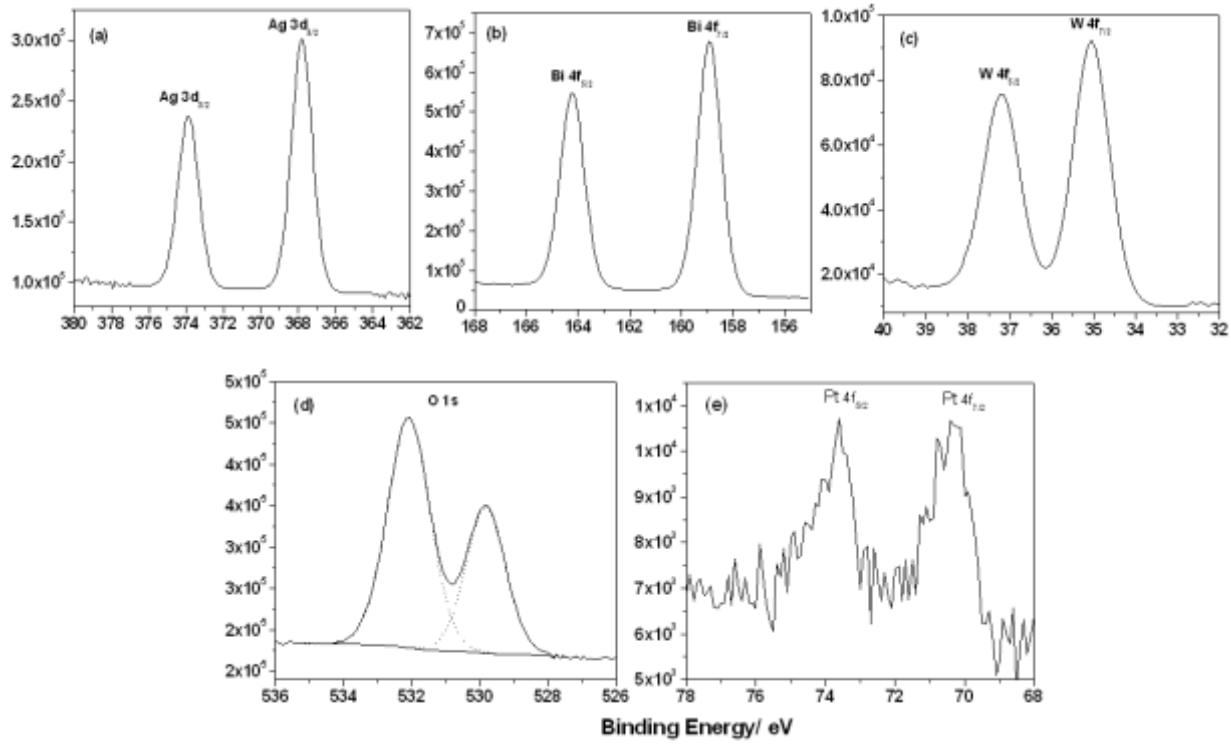

Figure 2.2.15 - High-resolution core level X-ray photoelectron spectra (ordinates in the spectra in counts per second) in the Ag 3d (a), Bi 4f (b), W 4f (c), O 1s (d) and Pt 4f (e) binding energy regimes for SCS-$AgBiW_2O_8$ (a-d) and Pt-modified SCS-$AgBiW_2O_8$.

in an oxide structure, with Bi^{3+} also surrounded by oxygen neighbors (such as in Bi_2O_3, Bi_2O_4), and with W^{6+} in a hexagonal oxygen-bonded structure (such as WO_3, H_2WO_4). The XPS data are in accord with a layered structure for $AgBiW_2O_8$ composed of WO_6 octahedral sheets interleaved with Bi-O-Bi layers and AgO_x polyhedra. Importantly, the XPS data also confirm that there is no *free* metal formation (i.e., Ag^0, Bi^0) during SCS synthesis. For example, in the Bi binding energy regime, the Bi $4f_{7/2}$ and Bi $4f_{5/2}$ signals in Figure **Figure 2.2.15b** are located at 158.95 and 164.2 eV; far higher in energy than the characteristic peaks for *metallic* Bi located at 156.8 eV and 162.2 eV respectively. Similar considerations apply for silver peaks as well.

In the O 1s binding energy regime (**Figure 2.2.15d**), the peak at 529.9 eV is in good agreement with that similarly reported for a bismuth tungstate structure and at variance with that for WO_3 at 530.5 eV. The other O 1s peak at 532.1 eV is assignable to residual water bound to the oxide nanoparticles and also to water molecules adsorbed on the sample surface.

Importantly, no changes were noted in the XPS profiles after use of the SCS-$AgBiW_2O_8$ sample in the dye photodegradation runs or after syngas generation attesting to the excellent photoelectrochemical stability of this oxide on band gap irradiation.

Figure 2.2.16 compares the temporal evolution (as assayed by GC) of the gaseous products for formic acid (**Figure 2.2.16a**) and acetic acid (**Figure 2.2.16b**) as the electron donor. A control with no initial Pt modification of the $AgBiW_2O_8$ powder is also included in the latter case (blue dash line). Control experiments conducted without the oxide semiconductor did not yield any of the products shown in **Figure 2.2.16** signaling that photolysis of the respective organic acid is not a factor here. It is also worth noticing that HCOOH performs as an in situ precursor for CO_2 generation (Figure **2.2.16** a).

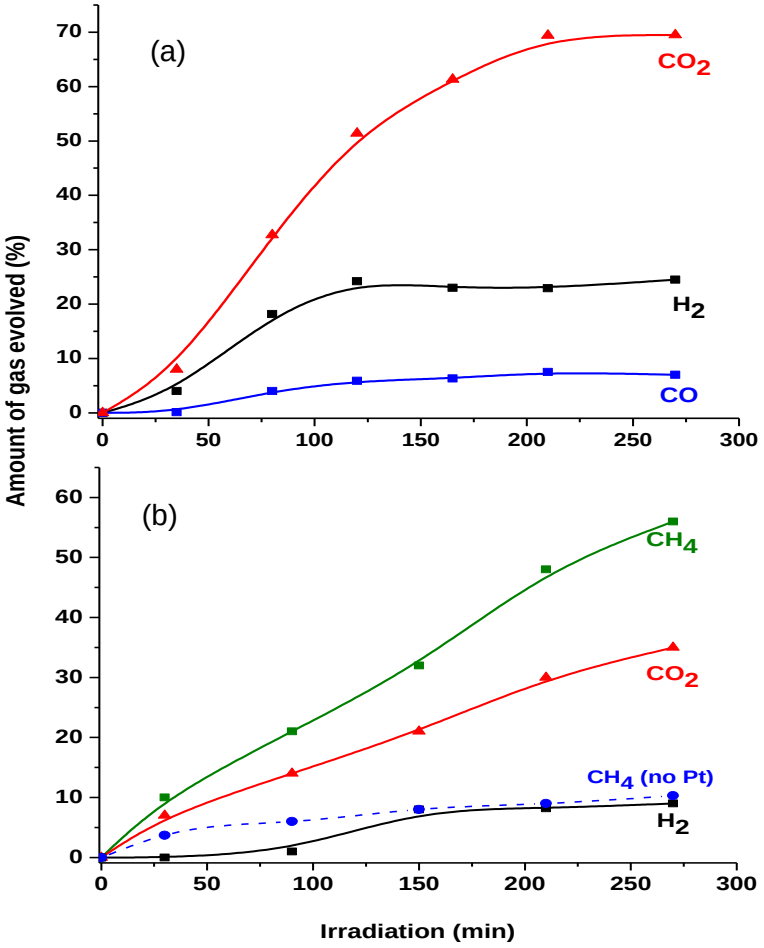

Figure 2.2.16 - Temporal evolution (as assayed by GC) of the gaseous products formed in the photocatalytic reaction of $AgBiW_2O_8$-Pt from formic acid (a) and acetic acid (b) as the electron donors. Both systems were saturated with N_2.

In fact, the direct electroreduction of CO_2 in aqueous media is hampered both by the low partial pressure of CO_2 in the atmosphere (3.9×10^{-4} atm) and by its low solubility in water (1.5 g/L at 298 K). On the other hand, formate species have high solubility in water (945 g/L at 298 K). Further, they have high proclivity for being adsorbed on oxide semiconductor surfaces and are easily oxidized by the photogenerated holes in the oxide semiconductor.

In both cases (**Figures 2.2.16a and b**), the photoreaction is initiated by photooxidation of the respective carboxylic acid (photo-Kolbe reaction) on the oxide photocatalyst surface. Competition by water photo-oxidation is expected only as a minor contribution and the $^{\bullet}OH$ radicals, generated from initial hole attack on adsorbed water molecules, are most likely involved in oxidation of the carboxylic acid than in O_2 generation. H_2 photogeneration on Pt sites occurs in both cases although initial Pt modification of the oxide surface has different consequences. In the case of formic acid as the electron donor, H_2 photogeneration is completely quenched in the absence of Pt while for acetic acid (**Figure 2.2.16b**), the extent of methane photogeneration is influenced by the presence of Pt islands on the oxide surface.

The above observations can be rationalized by invoking radical intermediates that are generated on initial photo-oxidation of the organic acid. **Figure 2.2.17** summarizes the mechanistic paths for the photocatalytic Kolbe reaction plus other reactions occurring on irradiation of Pt-modified SCS-$AgBiW_2O_8$ nanoparticles in contact with HCOOH (Figure **2.2.17**a) and H_3CCOOH (Figure **2.2.17**b) respectively. The intermediate $HCOO^{\bullet}$ radical generated in the first case (formic acid) by reaction with a photogenerated hole (in the oxide) then injects an electron into the $AgBiW_2O_8$ conduction band via the well-established current–doubling mechanism (see **Figure 2.2.17a**). The net result is formation of hydrogen atoms ($H^{\bullet}$on Pt sites followed by subsequent H_2 formation) and CO_2. In the second case for acetic acid, the corresponding $H_3CCOO^{\bullet}$ photogenerated radical (formed from initial hole attack on acetate) rapidly decomposes to $H_3C^{\bullet}$ + CO_2, and then the $H_3C^{\bullet}$ radicalsuse the hydrogen atoms stored on Pt islands to get ultimately converted into CH_4 (**Figure 2.2.17b**).If the Pt sites are absent, the surface reaction involving the methyl radicals and hydrogen atoms would be inhibited.

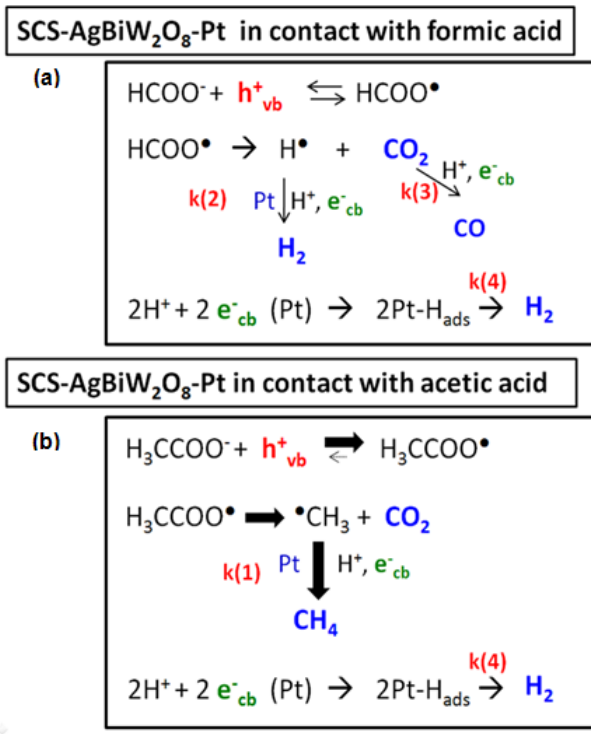

Figure 2.2.17 - Mechanistic pathways for the photocatalytic Kolbe reaction along with other reactions occurring on irradiation of Pt-modified SCS-$AgBiW_2O_8$ nanoparticles in contact with formic acid (a) and acetic acid (b) respectively.

What about trends in product

evolution in the (*dark*) electrochemical cases for the two acids considered here? The electrochemical oxidation of carboxylic acids (Kolbe reaction) proceeds through different paths depending on the anode material. On a platinum electrode and with simple carboxylic acids such as H_3CCOOH, the Kolbe reaction (induced, for example, by galvanostatic polarization) generates hydrocarbons through a free radical sequence as follows:

$$H_3CCOO^- \rightarrow H_3CCOO^\bullet \rightarrow H_3C^\bullet + CO_2$$
$$2\ H_3C^\bullet \rightarrow CH_3\text{-}CH_3$$

Thus, the *normal Kolbe reaction* involves radical-radical coupling ($H_3C^\bullet$ coupling) as the predominant mechanism at platinum anodes while an *abnormal Kolbe reaction* almost exclusively occurs at carbon electrodes either in organic or in aqueous media generating CH_3COOCH_3.With α-substituted carboxylic acids, more complex mechanisms involving radicals and/or carbonium ion intermediates give rise to the formation of other products such as olefins, alcohols, ethers, and esters.

Interesting contrasts have been reported in product evolution for similar electrode surfaces with and without illumination. Thus ethane was observed as the dominant product on a TiO_2*photoanode* in organic media (acetonitrile) with 0.1 M tetrabutyl ammonium perchlorate as supporting electrolyte and 0.08 M of tetrabutyl ammonium acetate as source of acetate ions.On the other hand, methane (rather than ethane) was reported on photoirradiated TiO_2-Pt nanoparticles in contact with acetic acid very similar to the observations in this study (**Figure 2.2.17b**). Methyl radical coupling (leading to ethane) is clearly favored on the massive electrode surface because of a site proximity effect.

Quantum yields for the formation of syngas (H_2+CO) and CO_2 in the formic acid solution were as follows: H_2 = 3.0 %, CO = 0.8 % and CO_2 = 4.5 %. [Chemical actinometry using an aqueous solution of 6 mM $K_3Fe(C_2O_4)_3.3H_2O$ in 1.0 N H_2SO_4 provided a calculated photon flux of 3.2 x 10^{-2} moles and thus the reported quantum yield was calculated as the percent ratio of the number of moles of product divided by the moles of photons.] The H_2:CO_2 ratio was seen to be ~ 1:1.5 for reaction times up to 1 hr, whereas it reached a ratio of 1:2.8 for reaction times higher than 3 h. Product amounts at the end of the photocatalytic runs were as follows:

$H_2 = 1.0 \times 10^{-2}$ mol/g.L
$CO = 3.0 \times 10^{-3}$ mol/g.L
$CO_2 = 2.8 \times 10^{-2}$ mol/g.L

These data are reported as the number of moles of product divided by the photocatalyst mass and liquid volume in the photoreactor. The turnover number (TON = molar amount of reacted electrons divided by molar amount of catalyst) for the photocatalytic formation of H_2 + CO (using a factor 2 to represent the number of electrons per H_2 and CO respectively) on the Pt-modified SCS-$AgBiW_2O_8$ nano-particles reached a value of ca. 4.3 after 4 h irradiation, producing 1.0 mmol of H_2 and 0.3 mmol of CO.

For the photocatalytic synthesis of CH_4 from acetic acid on Pt-modified $AgBiW_2O_8$ nanoparticles, the amount of gases generated at the end of the runs was:

CH_4 = 1.45 x 10^{-2} mol/g.L
CO_2 = 0.92 x 10^{-2}mol/g.L
H_2 = 0.24 x 10^{-2} mol/g.L

The quantum yields were as follows: CH_4 = 1.7 %, CO_2 = 1.2 % and H_2 = 0.3 %. The experimental CH_4:CO_2 ratio was found to be ~ 1.5:1 at reaction times up to 1 h, increasing slightly afterwards to 1.6:1.

Rate constants of the reactions associated with the photogenerated electrons are indicated as k(x) (with x = 1 to 4). The reaction product profiles are consistent with an ordering of these rate constants: k(1) > k(2) ~ k(4) > k(3). The very low amount of H_2 formed in the case of acetic acid is consistent with k(1) > k(4) which means that the photoelectrons are mainly consumed in the generation of CH_4 from the methyl radical. Importantly no C_2H_6 was found in our experiments indicating that the conduction band electrons are transferred to $H_3C^{\bullet}$thus cancelling out the radical-radical coupling. The uptake of e^-_{cb} from Pt-modified SCS-$AgBiW_2O_8$ is much higher by $H_3C^{\bullet}$ than by CO_2 (k(1) > k(3)) and therefore no CO is observed in the data for CH_3COOH (**Figure 2.2.16b**). Further, k(2) > k(3) which would be consistent with the ratio, H_2 : CO ~3: 1, measured for formic acid as the electron donor.

Competition by water photooxidation is expected only as a minor contribution and the $^{\bullet}OH$ radicals, generated from initial hole attack on adsorbed water molecules, are most likely involved in oxidation of the carboxylic acid than in O_2 generation. The main product in the acetic acid solution was methane and the extent of methane photogeneration was highly influenced by the presence of Pt islands on the oxide surface. H_2 photogeneration on Pt sites occurs in both cases although initial Pt modification of the oxide surface has different consequences. In the case of formic acid as the electron donor, H_2 photogeneration is completely quenched in the absence of Pt while for acetic acid, the extent of methane photogeneration is influenced by the presence of Pt islands on the oxide surface and accounting for ca. 4 times more amount of methane.A full paper reporting these results have been recently published in *ChemPhysChem(see Publication # 3 below).*

Photoreduction of CO_2using p-type Cu_2Oelectrodes and pyridine as co-catalyst

Copper (I) oxide, Cu_2O, is an attractive p-type semiconductor with a band gap energy of ~ 2.0 eV, a conduction band-edge lying far enough negative to sustain CO_2 reduction, and a high absorption coefficient over the wavelength range in the solar spectrum. Preparation of Cu_2O photocathodeswas performed byelectrodeposition on gold-coated quartz crystal working electrodes either at constant current or at constant potential using 0.2 M $CuSO_4$ + 3 M lactic acid + 0.5 M K_2HPO_4, pH 12 as the electrodeposition bathkept at 25 °C. Although there are quite a few studies on the use of Cu_2O photocathodes for HER, there are no reports to the best of our knowledge on their use for CO_2 photoreduction. An intriguing aspect for study hinges in the capability of preferentially oriented electrodeposited films for CO_2 photoreduction. Among the (100), (110) and (111) crystal faces of Cu_2O, the (111) orientation is the best one for photoreduction reactions and therefore the data presented below correspond to electrodeposited Cu_2O(111) films.

Our data below correspond to electrodeposited Cu_2O(111) films (as corroborated by XRD analysis) at –0.4 V up to reach a total charge of 180 mC/cm^2 which corresponds to 0.25 μm film thickness.The associated film mass was 140 μg/cm^2 as measured by electrochemical quartz crystal microgravimetry (EQCM).

To analyze the stability of electrodeposited Cu_2O(111) electrodes, cathodic photocurrent density (i_{ph}/cm^2) and mass change (Δm) as a function of potential under chopped simulated AM 1.5 solar illumination were recorded in a solution just containing the supporting electrolyte. Prior to defining the optimal film thickness, careful analyses were performed (data not shown) to verify compliance of the EQCM set-up with the Sauerbrey equation.

Figure 2.2.18 compares the effect of solar light intensity on the photocurrent and Δm values for the photoelectro-reduction of water to hydrogen. The data in **Figure 2.2.18**(top) are for illumination from 1.5 AM solar simulator, and those in **Figure 2.2.18** (bottom) are for the case when a 10% neutral filter was placed in between the light source and the electrochemical cell. Clearly, although significantly higher photocurrents (up to2 mA/cm^2) are reached under full illumination, there is a beneficial effect on the relative photocurrent and mass changes brought about by decreasing the light intensity. The total photocurrent is mainly associated with photoelectron transfer to water thus photogenerating H_2 as represented in Eqn. 3:

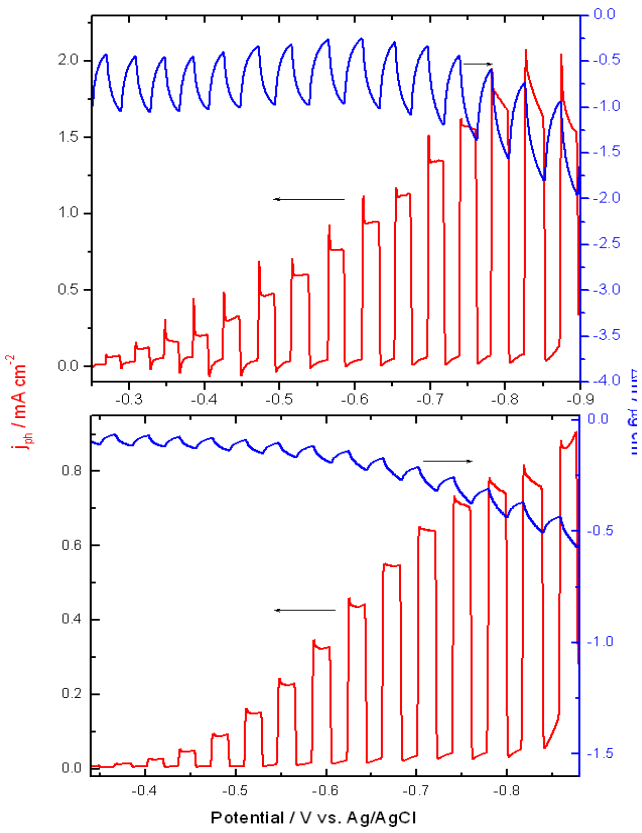

Figure2.2.18. Effect of light intensity on photocurrent/potential and Δm/potential profiles of Cu_2O films under chopped simulated AM 1.5 illumination at full output (top) and at 10% intensity with a neutral filter (bottom).

$$H_2O + 2e^- \rightarrow H_2 + 2\,OH^- \quad (3)$$

Nonetheless, there are also measurable mass changes associated principally with the photocathodic decomposition of the oxide as indicated in Eqn. 4:

$$Cu_2O + 2e^- + H_2O \rightarrow 2Cu + 2OH^- \quad (4)$$

The above data show that electrodeposited Cu_2O(111) films are more stable and reached higher photon to current conversion ratio than under the full output of simulated AM 1.5 illumination. This effect in performance seems to be rooted in the better capability of the photoelectrode/electrolyte interface to deal with a lower number of photons because: i) There is less photoconversion of Cu_2O to Cu^0 (Eqn. 4) as indicated

by a lower mass loss and ii) A more efficient transfer of photocurrent is associated with the transfer the photogenerated electrons to the electrolyte, i.e., conversion of water to H_2 (Eqn. 3) when the light intensity is low. It is useful to recall here that the minority-carriers (photoexcited electrons) are collected just over a distance corresponding to the sum of the space charge layer thickness and the electron diffusion length. For electrodeposited Cu_2O(111) electrodes, this distance is always less than 100 nm in the potential range under study, while the photon absorption depth near the band gap is much larger and in the micrometer range (1-2 μm).

For CO_2 reduction on illuminated Cu_2O(111), chopped (0.2 Hz) and continous AM 1.5 simulated solar illumination were used (**Figure 2.2.19**). The pH of the electrolyte was adjusted to pH 5 to compare CO_2 reduction in the absence and in the presence of protonated pyridine (PyH^+, pKa = 5.5) as solution co-catalyst. Chopped irradiation under -0.4 V (a rather low potential for Reaction 4 to be dominant) shows that the presence of PyH^+ enhances the cathodic photocurrent associated to CO_2 reduction just in ca. 15 % (compare **Figure 2.2.19** a and b). While the photocurrent enhancement by PyH^+ is in fact not really dramatic, the PyH^+ contribution by draining the photoelectrons to the solution side, thus avoiding the electrode photocorrosion, is quite clear as shown in the comparative mass changes under continous irradiation (**Figure 2.2.19** c). Observe that the rate of mass decrease is faster in the absence of PyH^+ reaching a total mass loss of 4.0 μg/cm^2 after 120 s of irradiation, while the presence of PyH^+ brought about a net lost of only 2.9 μg/cm^2 after 200 s.

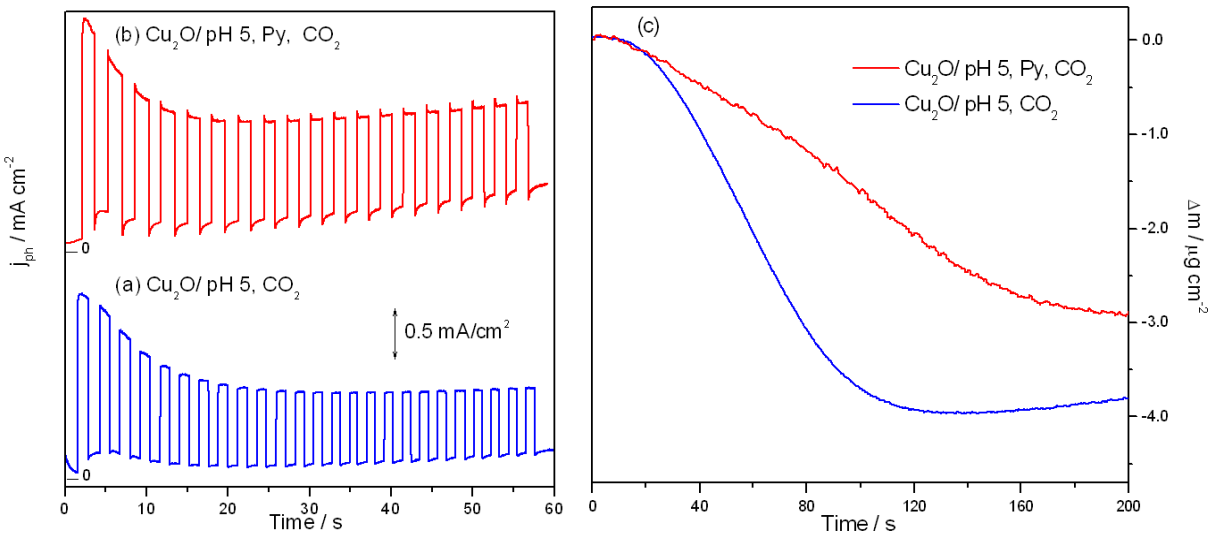

Figure 2.2.19 Photocurrent flow (under chopped 105 AM 1.5 illumination) at -0.4 V (vs. Ag/AgCl) for a Cu_2O(111) film in pH 5, CO_2 saturated solution without (a, blue line) and with (b, red line) 10 mM pyridine. (Curves were shifted for better comparison and each one includes the zero current). Frame (c) contains a comparison of mass changes (as measured by EQCM) for the respective (a) and (b) scenarios except that continuous instead of chopped irradiation was used.

Although these mass changes indicate the instability of the Cu_2O photoelectrodes, longer times of irradiation do not show more significant mass changes which in comparison to the total film mass (140 $\mu g/cm^2$) are only in the 2-3% range. Further, the presence of PyH^+ enhances the film inertness as indicated by the absence of mass increase associated with adsorption of solution species on the $Cu_2O(111)$ surface.Therefore, preparation variables for Cu_2O photocathodes were optimized for solar photoelectrocatalytic reduction of CO_2.Light intensity and solution co-catalyst concentration were adjusted to reach the highest photocurrent performance.

Publications/ Patents:

1. de Tacconi, N.R.; Chanmanee, W.; Dennis,B.H.; MacDonnell, F.M.; Boston, D.J.; Rajeshwar, K. **"Electrocatalytic Reduction of Carbon Dioxide Using Pt/C-TiO_2 Nanocomposite Cathode"***Electrochemical and Solid-State Letters*, **2011**, *15 (1)*, B5-B8.
2. Rajeshwar, K.; de Tacconi, N. R.; Timaji, H. K. **"New-generation Oxide Semiconductors for Solar Energy Conversion and Environmental Remediation"***J. Nano Research* **2012**, *17*,185-191.
3. de Tacconi, N. R.; Timaji, H. K.; Cahnmanee, W.; Huda, M. N.; Sarker, P.; Janaky, C.; Rajeshwar, K. **"Photocatlytic Generation of Syngas Using Combustion-Synthesized Silver Bismuth Tungstate"***ChemPhysChem***2012,** *13*, 2945-2955.
4. D. J. Boston, K-L. Huang, N. R. de Tacconi, F. M. MacDonnell and K. Rajeshwar, **Book chapter:Electro- and Photocatalytic Reduction of CO_2: The Homogeneous and Heterogeneous Worlds Collide?** in Photoelectrochemical Water Splitting: Challenges and New Perspectives **(**H-J. Lewerenz and L. M. Peter, eds.) RSC Press. In press.

Task 3: Coal to Liquids Catalyst Optimization

Several processes for converting lignite into synthetic crude (syncrude) were investigated by our group in previous projects. At that time, we developed a direct coal liquefaction (DCL) method based on a catalytic reaction conducted under moderate temperature and pressure conditions. Our ultimate goal is to bring this process to a pilot scale somewhere close to a lignite mine in Texas.

In support of this effort, we conducted bench-scale experiments with the goal of reducing overall catalyst cost by either increasing the catalyst reactivity thus reducing required concentrations or by using cheaper catalyst materials. In addition to the catalyst development, we investigated the impact of process conditions on the yield of the process. The yield was also investigated as a function of feedstock. In this project, lignite feedstocks mined from East Texas and from the Labtrobe Valley in Australia were used. A process to reduce the inorganic (ash) content of the coal was developed in an effort to widen the acceptable range of feedstocks for the process. Finally, several liters of synoil were produced using our DCL process.

The experiments for evaluating catalysis and process conditions were performed in our laboratory. Our bench top setup was composed of two batch reactors with 450 mL capacity and a larger 2.0 gallon batch reactor. The 450 mL reactor was used to conduct the parameteric experiments throughout the project. The 2.0 gallon reactor was used towards the end of the project to produce several liters of synoil.

The parametric catalyst experiments were performed using the following steps. The catalyst and Texas lignite coal were loaded into a 450mL pressure reactor containing a lignite derived solvent. The mixture was heated rapidly while stirring for a fixed time under H_2 pressure. Once the target residence time was reached, the reactor was rapidly cooled by running water through an internal coolant loop. The resulting slurry was diluted with tetrahydrofuran (THF) and passed through a filter. The solid residue on the filter, which was a mixture of unreacted coal and catalyst, was washed with THF, dried, and weighed. The THF was removed from the filtrate by rotatory vacuum distillation. The resulting THF-free oil product was then weighed. The oil yield was determined by subtracting final oil weight from the initial solvent oil weight.

For purposes of making fair comparisons between feedstocks, the yield in this report will be presented as a percentage yield that is taken on a moisture and ash free (maf) basis. This is computed by taking the mass of the net synoil product and dividing by the sum of the volatile and fixed carbon mass in the feedstock, which is determined from the proximate analysis.

The percent conversion is computed by dividing the mass of the unreacted coal by the sum of the volatile and fixed carbon mass in the feedstock. In some circumstances the yield may be low but the conversion may be high. This can happen when the reaction products are gases rather than liquids.

Catalyst Development

The initial stages of the project were focused on identifying active catalysts for the process with the goal of reducing cost. From our previous work, we had known that noble metals, such as palladium, were effective, although costly catalysts. In that previous work, the noble metal was dispersed on a carbon powder support and mixed with the coal and the solvent during the reaction. The fine powder made for good dispersion and high reaction area but was nearly impossible to separate for reuse. We therefore focused on powders with larger granules (~150 mesh) and composed of cheaper materials like metal oxides (silica, alumina, and iron oxides), which are relatively cheap and potentially disposable.

Parameters that were varied include the size and composition of the support, the metal loading on the support, and type of metal. The catalysts were prepared in our laboratory using commercially available supports. The candidates were tested for yield according to the procedure outlined in the previous section. From these studies, we identified two proprietary catalysts (denoted as BXF1 and BFX9) that gave largest synoil yields for the process conditions that were tested.

The synoil produced using BXF1 was subjected to simulated distillation with a GC-FID and compared with commercial diesel fuel (Figure 3.1). The results show the synoil contains a significant diesel-like fraction. The heavier portion is composed of aliphatic and aromatic compounds that could be further processed by conventional oil refining techniques. The product yield and quality for BXF1 was found to be acceptable, so we decide to use BXF1 for the remainder of the project studies.

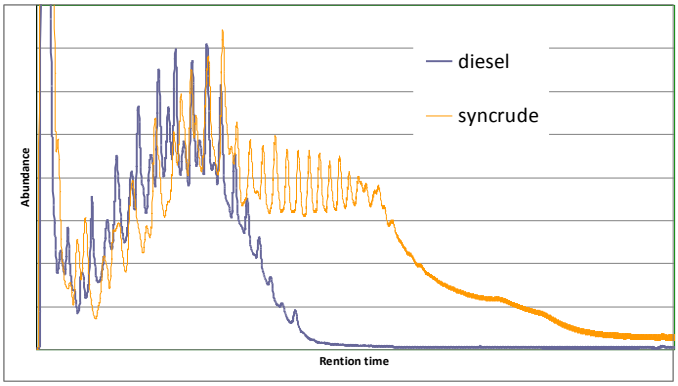

Figure 3.1: Comparison of synoil produced using BXF1 with diesel fuel

Process Conditions

A series of parametric experiments were designed to determine the effect of process conditions such as temperature, pressure, coal moisture content, and coal to catalyst ratio. We focused on one sample of coal (Texas Lignite 2 or L2) for these parametric studies.

The effect of catalyst loading on the synoil and conversion yields was studied first. As shown in Figure 3.2, reactions involving 0 to 16 mass percent catalyst were performed on lignite samples in the solvent. Yields increased with catalyst loading up to 12 mass % after which no further increases were observed. The synoil yield peaked at 45% with a corresponding 80% conversion overall. Higher loadings do not further improve the yield and are avoided so as to minimize catalyst. The initial drop in conversion yield upon addition of BXF1 was counterbalanced by an increase in liquid yield, indicating that the presence of the catalyst inhibited gasification and favors liquefaction.

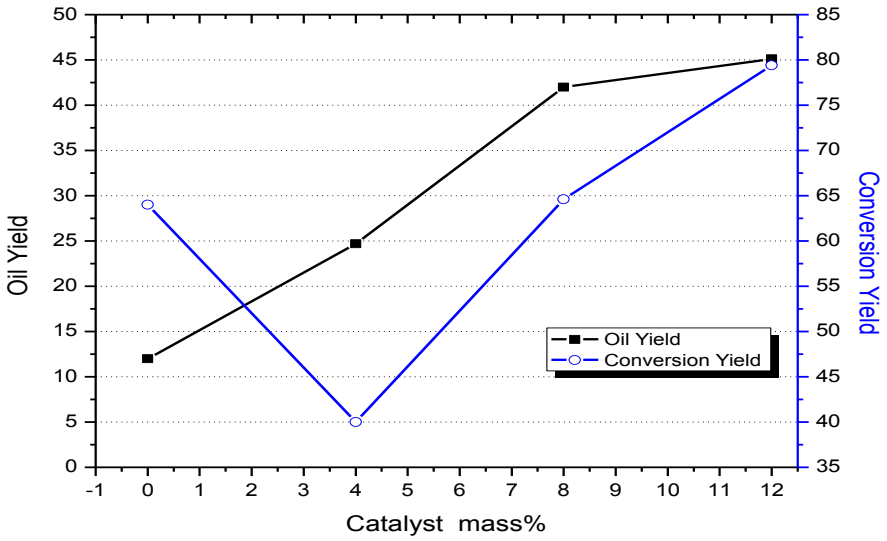

Figure 3.2: Effects of catalyst loading on coal liquefaction under normal conditions

Next, the effect of moisture content on the synoil yield was studied. The coal moisture is categorized as free water and water formed upon the decomposition of the coal structure. To control the moisture content, we chose to focus on removal of free water.

First, we evaluated different processes to dry the coal to the desired level of moisture. These included drying in an oven with air, drying in an oven with nitrogen, drying in a vacuum oven, and drying *in situ* with hydrogen. We found that the drying procedure impacted the yield of the synoil regardless of the amount of moisture removed. The best yields were obtained using the vacuum oven at low temperatures. The worst were obtained when air drying was used.

A systematic process was then developed for drying the coal to the desire moisture percentage. First, the level of moisture in the coal was determined by using thermo gravimetric analysis (TGA). The necessary time need for drying was then calculated using an empirical formula. The formula was obtained using the moisture level (determined by TGA) of small samples taken periodically from coal that was vacuum dried for a fixed length of time.

The lignite coals typically contained 20%-30% moisture and we found that drying to 10% moisture gave the best yields on a moisture and ash-free (maf) basis (Figure 3.3). Gas yield is minimized between 10 and 20% moisture, where liquid yields are maximized, showing an obvious optimal condition for the DCL process.

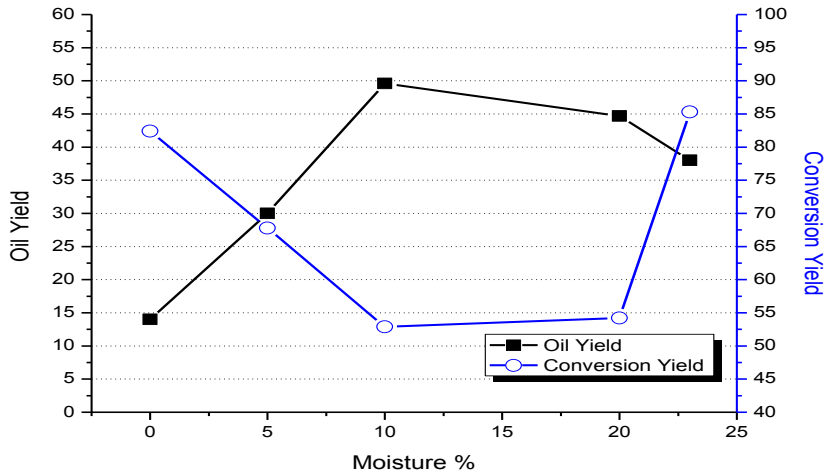

Figure 3.3: Effect of moisture % on coal liquefaction under normal reaction conditions.

The process temperature effect on yield and conversion was studied over the range of 100^{o}C. For the highest temperature, the conversion increased to 45% compared to 30% for the lowest temperature. However, the yield dropped from 40% to 20% at the high temperature. We therefore conclude that increasing the reaction temperature shifts the selectivity towards gaseous products rather than liquid ones.

Similarly, the hydrogen partial pressure effect on yield was studied over a 700 psig range. At the higher pressure the conversion increased to 35% compared to 25% for the low pressure. However, synoil yield remained relatively constant indicating that gasification increases with increased pressure.

Impact of Feedstock

During the course of the project we tested the influence of lignite feedstocks on yield. The proximate analysis of different lignite feedstocks were performed using TGA and are given in Table 3.1. The feedstocks represent a wide range of ash levels from 1% to 18%.

Table 3.1: Lignite feedstocks tested

Lignite	% moisture	% volatiles	% fixed carbon	% ash
Australian	21	40	38	1
TX lignite 1 (L1)	28	22	32	18
TX lignite 2 (L2)	30	29	33	9
AR lignite	34	39	20	7
TX lignite 3 (L3)	24	31	34	11
Low Ash TX Lignite (LAL)	23	28	40	9

Results such as synoil yield and synoil quality (gravity, boiling point distribution, H/C ratio) were evaluated for each run. In addition, lignite feedstocks with variability in ash were evaluated to gage sensitivity to inorganics. The coal samples were dried to 10% moisture according to the procedure developed previously. Optimal pressure and temperature determined previously were used for each case. We found the product quality such as H/C ratio and boiling point distribution to be relatively insensitive to feedstocks tried. The yield and the estimated product volume per maf ton and as received (ar) ton are given in Table 3.2.

Table 3.2: Yield for different feedstocks with BXF1 catalyst

Coal	maf Oil Yield %	bbl/maf ton	bbl/ar ton
Australian	45 %	3.51	1.33
L1	27 %	2.12	1.25
L2	58 %	4.56	2.77
L3	60 %	4.72	3.03
LAL	38 %	2.99	1.02
AR lignite	33 %	2.59	1.53

We note that the coal L1 has the highest ash level and has the lowest yield. The AR coal gave a relatively low yield compared to other coals with similar proximate analysis. We attribute this to the fact that the coal sample was taken from a coal batch that was mined more than ten years ago and left on surface. The sample was likely oxidized after being exposed to the atmosphere over the years.

Ash Reduction

The level of ash content was found to have a significant impact on the yield of the synoil product. In order to widen the process to higher ash feedstocks, we investigated methods for reducing the ash content in the lignite feedstocks. The coal NRG2 with a 30% ash content (on wet basis) was used as the base coal. Two approaches were used. First, we investigated a washing technique using a combination of surfactant and frothing agent. The ground coal particles were mixed with water and then subjected to sonication to release ash particles from the coal matrix. The slurry was mixed with a frothing agent and a detergent to modify the surface properties of the ash and coal particles. Bubble washing was using to create surface foam that captured the coal particles. Though the ash was reduced on the floated particles, a significant amount of coal sank to the bottom of the washing container.

Another approach to reduce the amount of carbon rejected with the ash was developed. The method is based on a mixture of dilute acids. The coal particles are insoluble in the mixture while metal oxides are dissolved. The slurry was heated slightly, stirred for several minutes, and then poured through filter paper. The collected solids were then washed with water and dried. The ash levels were reduced by more than 50% with no loss of carbon material. The treated coal was then subjected to digestion with BXF1 catalyst with expected yields. The pretreated coal samples were dried to 10% moisture according to the procedure developed previously. Optimal pressure and temperature determined previously were used for each case. Results such as synoil yield and synoil quality (gravity, boiling point distribution, H/C ratio) were evaluated for each run.

Some effort was spent trying to reduce the cost of the acid wash method by reducing residence time, reducing the amount of acid, and using lower cost acids. Temperatures up to 50^{o}C were tested to determine the reduction in residence time. In addition, we investigated different acids including HF, H_2SO_4, H_2SO_3, HCl, and HNO_3. The goal was to create an ash reducing wash that is economical on a commercial scale.

We considered the acid cost along with its ash reducing capability. We found HF to have the best ash reducing capability but the cost and safety issues made it uneconomical for use at the commercial scale. A dilute mixture of H_2SO_3 and HNO_3 was found to give a good balance between ash reducing capability and cost. In all cases the treated coal was then subjected to digestion with BXF1 catalyst with expected yields. The pretreated coal samples were dried to 10% moisture according to the procedure developed previously. Optimal pressure and temperature determined previously were used for each case. Results such as synoil yield and synoil quality (gravity, boiling point distribution, H/C ratio) were evaluated for each run.

We found the dilute mixture of H_2SO_4 and HNO_3 was able to significantly reduce the ash for less than $10 per barrel of synoil produced. The washed coal was tested with the catalyst BXF1. Yield performance was evaluated and found to be improved compared to the unwashed coal.

Production of Several Liters of Synoil

The last part of the project focused on producing several liters of synoil that could be evaluated by an external lab for quality and possibly for valuation. The results from this testing will be used in the future to evaluate the quality of the oil produced by the process, which is essential for any future economic analysis that would be done prior to commercialization.

Several months were spent designing, constructing, and using a large scale pyrolysis reactor for producing solvent. The outdoor reactor was composed of a 50-gallon drum that was wood fire heated from the bottom and surrounded by an insulating kiln. The drum outlets to a 15 foot packed steel condenser that terminated in a gas-liquid separation vessel. The gas removed from the top of the vessel was returned to the fire to eliminate odors. Water and oil were collected at the bottom of the vessel. With this approach, we were able to make hundreds of milliliters of solvent per run.

In addition to this work, we investigated different methods for separating the synoil from the unreacted solids in the slurry obtained after the digestion. One approach tested was vacuum filtration using a pocket leaf filter (PLF). The PLF is a jacketed filter that can be heated in order to reduce the viscosity of the slurry. Starting from a 20% slurry, the PLF produced a cake with 80% solids. Though this recovered enough oil to be used for a second cycle of digestion, it could only operate with 60g of slurry per run making it impractical to use with the ~800g of slurry produced by a single run of our digestion in the 2.0 gallon reactor. For this reason, we decided to stay with our standard THF extraction method and use a second rotary evaporator to speed up the separation of the THF and the synoil. The solid particles were removed from the synoil-THF mixture with a series of metal sieves and then finally passing it through a high flow rate hydraulic oil cartridge filter to remove particles greater than 10 μm.

The acid washing procedure was used to prepare around 10 lbs. of low ash Texas lignite that was then used for the digestions. In addition, some time was spent preparing large amounts of BXF1 catalyst for the digestion reactions. Once the coal and catalyst were prepared, we commenced digesting the coal in the solvent, and then extracting the synoil from the unreacted coal using the THF approach. The THF was removed from the synoil using a rotary evaporator. The digestions were performed in a 2-gallon pressure reactor located in our laboratory at a rate of approximately two runs per week.

The recovered synoil was then cycled twice more to assess the effect of recycling on the oil. Samples were taken for elemental and simulated distillation tests for each stage in the cycling. By the end of the project, we had produced slightly more than three liters of synoil that had been used in three consecutive digestions. This oil will be sent to an external lab for fractionating and testing of the fractions at some point in the future.

Synoil Characterization

The synoil produced was evaluated using various tests performed in our university and some by external labs. We focused our analysis on whole crude properties rather than tests on specific fractions due to the small amount of synoil product available.

The elemental composition is the most fundamental characteristic of any oil. The CHNOS mass percentage is for the synoil is given in Table 3.3. We compare our results with those for a generic crude oil. The synoil is high in oxygen content compared to the crude, which is not surprising considering the lignite feedstock contains a significant amount of oxygen. The sulfur content is low compared to "sour" crudes that have a sulfur content greater than 0.5%.

Table 3.3: Elemental analyses of Products of UTA synoil.

Elements	Crude Oil	UTA Crude (average)
Carbon	83 to 87 %	81-84 %
Hydrogen	10 to 14% (H/C 1.7)	9.88 % (H/C 1.4)
Nitrogen	0.1 to 2%	0.44 %
Oxygen	0.05 to 1.5% (O/C 0.007)	5.78 % (O/C 0.052)
Sulfur	0.05 to 6.0%	0.645 %

The synoil was subjected to simulated distillation (SIMDIST) following ASTM D7169 to determine the distillation curve using gas chromatography (GC). The SIMDIST data reveals that generally 95% of the synoil can be distilled at temperatures below 550^{o}C. The simulated distillation curve of the synoil is plotted and compared with similar data taken from the literature (Figure 3.4). The plot shows the synoil is somewhere between light and heavy crude, from a boiling point distribution perspective. The synoil does not appear to have a significant percentage of low or high boiling fractions, which results in a curve with a low slope relative to the curves for the crude oils.

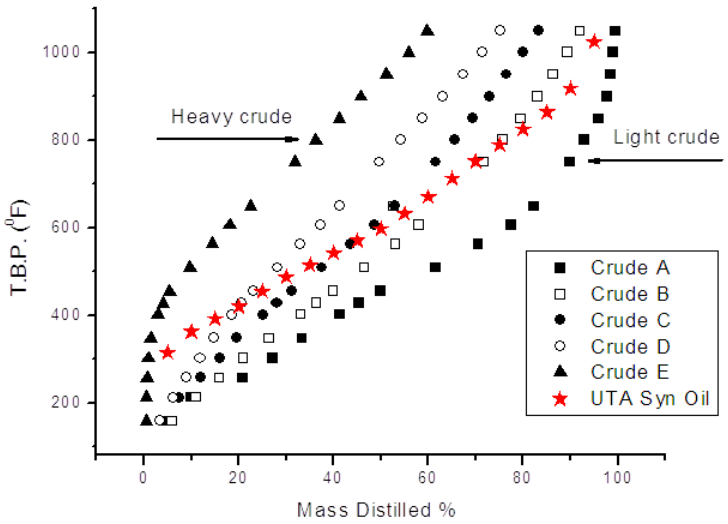

Figure 3.4: Simulated distillation T.B.P. curve in mass of UTA synoil compared to five types of crude oil ranging from light to heavy from Roussis, S. G.; Fitzgerald, W. P., *Analytical Chemistry*, **2000**, 72, 1400.

Additional properties with comparison to heavy crudes are given in Table 3.4. The synoil has an API gravity of 9.8^{o} yet has boiling points and kinematic viscosity that are comparable with medium crudes (25-30^{o}API). As shown in the table, the heavy crudes have higher gravity yet have higher viscosities, sulfur content, vanadium than the synoil.

Table 3.4: Comparison between UTA synoil and crude oils bulk properties.

Oil Type	Gravity (°API)	Sulfur (wt%)	Kinematic Viscosity at 100 °F (cSt)	Vanadium (ppm)	Total Acid Number (mg KOH/g)	Pour point (°C)
Bachaquero-13*	12.2	2.8	48.6	442	3.13	-18
UTA synoil (Data from PTI/Intertek Labs)	9.8	0.59	36	0.4	2.85	-18
Boscan*	10.1	5.4	11233	11222	0.91	7
Maya[1]	21.5	3.4	170@77F	277.5	0.43	-30

* http://www.genesisny.net/Commodity/Oil/OSpecs.html
[1] "Guide to World Crudes: Four Mexican crude assays updated," *Oil & Gas Journal*, May 15, 2000.

We speculate that the low gravity is due to the presence of low molecular weight aromatic and oxygenated compounds, such as phenols. These compounds, which are not typically found in petroleum, have a high density but low boiling points. The presence of these compounds can also explain the high acid number relative to the crude oils. We would conclude that the API gravity is not a representative number for the value or quality synoil as it does not correlate with high value characteristics of the synoil, mainly it's low boiling points, low viscosity, low sulfur, and lack of high residual content.

PROJECT COSTS

The project was completed within planned budgets. Cost summaries are listed in Table 1 below and Table 1a on the next page.

Table 1

	Start: January 2011			End: January 2013			
	Q4 2010	Q1 2011	Q2 2011	Q3 2011	Q4 2011	Q1 2012	Q2 2012
Baseline Cost Plan							
Federal Share	$0	$227,181	$246,824	$242,694	$244,302	$0	$0
Non-Federal Share	$0	$74,077	$46,049	$74,084	$46,042	$0	$0
Total Planned	$0	$301,258	$292,872	$316,777	$290,343	$0	$0
Cumulative Bseline Costs	$0	$301,258	$594,130	$910,907	$1,201,250	$1,201,250	$1,201,250
Actual Incurred Costs							
Federal Share	$0	$12,710	$92,753	$171,919	$181,435	$318,060	$136,876
Non-Federal Share	$0	$0	$0	$0	$ 83,932	$24,854	$80,924
Total Incurred Costs Qtrly	$0	$12,710	$92,753	$171,919	$265,367	$342,914	$217,800
Cumulative Incurred Costs	$0	$12,710	$105,463	$277,382	$542,749	$885,663	1,103,463
Variance							
Federal Share	$0	$214,471	$154,071	$70.775	$ 62,867	($318,060)	($136,876)
Non-Federal Share	$0	$74,077	$46,049	$74,084	($37,890)	($24,854)	($80,924)
Total Variance Qtrly	$0	$288,548	$200,120	$144,859	$ 24,977	(342,914)	($217,800)
Cumulative Variance	$0	$288,548	$488,668	$633,527	$658,504	$315,588	$97,789

Table 1a

	Q3 2012	Q4 2012	Q1 2013
Baseline Cost Plan			
Federal Share	$0	$0	
Non-Federal Share	$0	$0	
Total Planned	$0	$0	
Cumulative Bseline Costs	$1,201,250	$1,201,250	$1,201,250
Actual Incurred Costs			
Federal Share	$90,844	$55,540	$27,326
Non-Federal Share	$50,540	$0	$0
Corrections of Federal Incurred Costs from past financial reports	($126,464)		
Cumulative Incurred Costs	$1,118,383	$1,173,924	$1,201,250
Variance			
Federal Share	($90,844)	($55,540)	$0
Non-Federal Share	($50,540)	$0	$0
Total Variance Qtrly	($141,384)	($55,540)	$0
Cumulative Variance	$82,867	$27,326	$0

SCHEDULE/MILESTONE COMPLETION

All of both Task 2 and Task 3 have been completed. A no-cost extension of two weeks (to January 15, 2013) was asked of DOE and was granted to complete final experiments screening lignite samples.

Task	Milestone	Goal	Proposed Start	Proposed End	Revised Start	Revised End
2.1	Ligand Synthesis	Synthesize and characterize at least 500 mg of the desired phenanthroline ligands	Jan 1, 2011	May 30, 2011	Jan 1, 2011	March 31, 2011
	Ruthenium complexes-Ligand assembly	Complete the preparation and characterization of the Ru complexes.	April 1, 2011	July 30, 2011	April 1, 2011	June 30, 2012
	Solution and ITO surface photophysical measurements	Establish the photophysical properties of the photocatalysts in solution and adsorbed onto an ITO surface	April 1, 2011	October 30, 2011	August 1, 2012	March 30, 2012
	Photoelectrochemical cell construction and testing	Complete assembly of photoelectrochemical cell for the simultaneous oxidation of water and reduction of CO_2.	Sept 1, 2011	December 30, 2011	June 1, 2012	December 30, 2012
	Testing for photoelectron current	Different configurations and surface preparations	Oct 1, 2011	December 30, 2011	Sept 1, 2012	December 30, 2012
	Testing for photocatalysis and optimization	Testing for CO_2 reduction in complete cell	Nov 1, 2011	December 30, 2011	Oct 1, 2012	December 30, 2012
2.2	Prepare Pd-C-TiO_2 nanocomposite electrocatalysts	Develop preparative methods for nanocomposite syntheses and make materials for testing		April 15, 2011	Jan 1, 2011	June 15, 2011
	Characterize and test nanocomposite electrocatalysts	Characterization by SEM and XPS spectroscopy. Testing by electrochemical methods		December 30, 2011	March 1,2011	December 30, 2011
	Performance comparisons and testing for dark CO_2 reduction	Test nanocomposites for CO2 photoreduction and compare performance		May 30, 2011	June 15, 2011	May 30, 2012
	Demonstrate the viability of selected metal-loaded semiconductor nanostructures	Optimize cathode and anode nanocomposite materials		December 30, 2011	March 30, 2012	October 30, 2012
	Demonstrate the viability of 2-compartment cell approach to simultaneous photooxidation and CO_2 reduction.	Assemble test cell and testing for CO_2 photoreduction and water oxidation.		December 30, 2011	June 30, 2012	December 31, 2012

	Assemble the cell and test performance with with selected photoanode and cathode materials for CO_2 conversion efficiency.			December 30, 2011	Aug 30, 2012	December 31, 2012
3	Reactor set-up completed and testing begun.	Demonstrated operation of the test reactor. Complete catalyst screen for activity and lifetime. Make initial down selection.	Jan 1, 2011	May 1, 2011	Feb 1, 2011	May 1, 2011
	Complete screen of promoters/ co-catalysts	Down select to most promising catalyst configurations. Evaluate impact of process and catalyst on quality and quantity of synoil.	May 1, 2011	August 30, 2011	May 1, 2011	March 30, 2012
	Complete screen of feedstocks	Completed screen of Lignite samples. Assess robustness of catalyst and process to variation in feedstocks.	August 30, 2011	December 15, 2011	March 30, 2012	January 15, 2013
	Write final report	Complete final report based on results obtained during the entire Task 3	Novemb er 30, 2011	December 31, 2011	December 15, 2012	January 15, 2013